Available online at www.sciencedirect.com
SCIENCE DIRECT®
Physics Reports 409 (2005) 47–99
PHYSICS REPORTS
www.elsevier.com/locate/physrep

Raman spectroscopy of carbon nanotubes

M.S. Dresselhaus[a,*], G. Dresselhaus[b], R. Saito[c], A. Jorio[d]

[a] *Department of Physics and Department of Electrical Engineering and Computer Science, Massachusetts Institute of Technology, Room 13-3005, Cambridge, MA 02139, USA*
[b] *Francis Bitter Magnet Lab, MIT, Cambridge, MA 02139, USA*
[c] *Department of Physics, Tohoku University, and CREST, JST, Sendai 980-8578, Japan*
[d] *Depto. de Física, Universidade Federal de Minas Gerais, Belo Horizonte - MG 30123-970, Brazil*

Accepted 21 October 2004
editor: D.L. Mills

Abstract

The use of Raman spectroscopy to reveal the remarkable structure and the unusual electronic and phonon properties of single wall carbon nanotubes (SWNTs) is reviewed comprehensively. The various types of Raman scattering processes relevant to carbon nanotubes are reviewed, and the theoretical foundations for these topics are presented. The most common experimental techniques used to probe carbon nanotubes are summarized, followed by a review of the novel experimental findings for each of the features in the first order and second order Raman spectra for single wall carbon nanotubes. These results are presented and discussed in connection with theoretical considerations. Raman spectra for bundles of SWNTs, for SWNTs surrounded by various common wrapping agents, and for isolated SWNTs at the single nanotube level are reviewed. Some of the current research challenges facing the field are briefly summarized.

PACS: 78.; 78.67.Ch; 78.55.−m; 78.30.−j; 78.30.Na

Keywords: Carbon nanotubes; Graphene; Raman scattering; Photoluminescence

* Corresponding author. Fax: +1 617 253 6827.
E-mail address: millie@mgm.mit.edu (M.S. Dresselhaus).

0370-1573/$ - see front matter © 2004 Elsevier B.V. All rights reserved.
doi:10.1016/j.physrep.2004.10.006

Contents

1. Introduction . . . 49
2. Background . . . 50
2.1. Structure and notation . . . 50
2.2. Electronic structure . . . 52
2.3. Phonon structure . . . 55
3. Classification of Raman scattering processes . . . 56
3.1. First-order Raman scattering in the G-band and RBM of SWNTs . . . 57
3.2. Resonance and non-resonance Raman scattering . . . 58
3.3. Second-order Raman scattering, D- and G'-band . . . 59
3.4. Intravalley or intervalley DR Raman scattering . . . 60
3.5. Stokes or anti-stokes Raman scattering . . . 61
3.6. Breit–Wigner–Fano lineshape . . . 61
3.7. Summary of phonon mode classifications . . . 62
4. Resonance Raman intensity calculations . . . 62
4.1. Formulation of the Raman intensity . . . 63
4.2. Selection rules for Raman scattering . . . 64
4.2.1. Symmetry of electron and phonon wavefunctions . . . 64
4.2.2. Geometry of Raman observations . . . 64
4.2.3. Selection rules for optical transitions . . . 64
4.2.4. Selection rules of first-order Raman processes . . . 65
4.2.5. Circularly polarized light and light polarized normal to tube axis . . . 66
4.2.6. Selection rules for combination modes . . . 67
4.3. Electron–photon matrix elements . . . 67
4.3.1. Node for optical transitions in 2D graphite and SWNTs . . . 68
4.3.2. Diameter and chirality dependence of optical processes . . . 69
4.4. Electron–phonon matrix elements . . . 70
4.4.1. Electron–phonon scattering for first-order processes . . . 70
4.4.2. Inter-valley electron–phonon scattering . . . 71
4.4.3. Non-radiative relaxation of electrons . . . 72
5. Raman spectroscopy experiments for carbon nanotubes . . . 73
5.1. Sample preparation . . . 73
5.2. Micro-Raman spectroscopy . . . 74
5.3. Raman spectra data analysis . . . 75
6. Learning about carbon nanotubes from their first-order Raman features . . . 76
6.1. The radial breathing mode . . . 76
6.1.1. The RBM frequency and nanotube diameter . . . 76
6.1.2. The I_{RBM} and the electronic structure . . . 77
6.1.3. The RBM and the (n, m) assignment . . . 79
6.1.4. RRS vs. PL and environmental effects on RBM spectra . . . 81
6.2. The G-band . . . 82
6.2.1. The G-band lineshape and diameter dependence . . . 82
6.2.2. Polarization analysis . . . 84
7. Learning about carbon nanotubes from their double-resonance Raman features . . . 85
7.1. Overview of double resonance spectral features . . . 85
7.2. Analysis of the G' band spectra . . . 86
7.3. SWNT electronic structure obtained by G'-band studies . . . 86
7.4. Phonon trigonal warping effect . . . 88
7.5. Characterization of structural modifications of the nanotube sidewalls . . . 89

7.6. Overtones and combination modes above the *G*-band frequency 89
7.7. Combination modes with frequencies between the RBM and *G*-band 90
8. Multi-wall carbon nanotubes—MWNTs 92
9. Summary and future directions 93
Acknowledgements 95
References 95

1. Introduction

Carbon nanotubes have proven to be a unique system for the study of Raman spectra in one-dimensional systems, and at the same time Raman spectroscopy has provided an exceedingly powerful tool for the characterization of single-wall carbon nanotubes. The unique optical and spectroscopic properties observed in single-wall carbon nanotubes (SWNTs) are largely due to the one-dimensional (1D) confinement of electronic and phonon states, resulting in the so-called van Hove singularities (vHSs) in the nanotube density of states (DOS) [1,2]. These singularities in the DOS, and correspondingly in the electronic joint density of states (JDOS), are of great relevance for a variety of optical phenomena. Whenever the energy of incident photons matches a vHS in the JDOS of the valence and conduction bands (subject to selection rules for optical transitions), one expects to find resonant enhancement of the corresponding photophysical process. Owing to the diverging character of vHSs in these 1D systems, such an enhancement can be extremely confined in energy (meV), appearing almost like transitions in a molecular system. In combination with the unique 1D electronic structure, the resonantly enhanced Raman scattering intensity allows one to obtain detailed information about the vibrational properties of nanotubes, even at the isolated individual SWNT level [3].

The contents of this review are as follows. Section 2 provides the background for discussing the Raman effect in carbon nanotubes, summarizing the nanotube geometrical structure, as well as the electronic and vibrational (phonon) structure. Section 3 presents the different aspects of the Raman scattering processes, such as first- and second-order scattering, resonant and non-resonant scattering, Stokes or anti-Stokes scattering, intravalley or intervalley scattering, other elementary excitations and the parameters for Raman measurements. Section 4 discusses resonance Raman intensity calculations, including the formulation of the Raman intensity, selection rules for the Raman scattering, electron–photon matrix elements and electron–phonon matrix elements. Section 5 presents a brief description of sample preparation and the experimental set up. Sections 6 and 7 summarize Raman scattering experimental results, respectively for first- and for second-order Raman features. In Section 6 the radial breathing modes (RBMs), the (n, m) assignment that defines the uniqueness of each SWNT, and the *G*-band (tangential modes) are discussed. In Section 7, the *D*-band (disorder-induced feature) and the G'-band (*D*-band overtone) are given, as well as other double resonance features and the effects on the Raman spectra of interactions of SWNTs with their surroundings. Finally in Section 8 we mention MWNTs, and Section 9 presents concluding remarks, summarizing past achievements in the field and pointing to promising directions for future developments.

2. Background

2.1. Structure and notation

This section provides a brief introduction to the unusual structural properties of single-wall carbon nanotubes, that emphasizes their unique 1D attributes and sets them apart from other materials systems. A SWNT can be described as a single layer of a graphite crystal that is rolled up into a seamless cylinder, one atom thick, usually with a small number (perhaps 10–40) of carbon atoms along the circumference and a long length (microns) along the cylinder axis [4]. Each SWNT is specified by the chiral vector $\mathbf{C}_h$

$$\mathbf{C}_h = n\mathbf{a}_1 + m\mathbf{a}_2 \equiv (n, m) \tag{1}$$

which is often described by the pair of indices (n, m) that denote the number of unit vectors $n\mathbf{a}_1$ and $m\mathbf{a}_2$ in the hexagonal honeycomb lattice contained in the vector $\mathbf{C}_h$. As shown in Fig. 1, the chiral vector $\mathbf{C}_h$ makes an angle θ, called the chiral angle, with the so-called zigzag or $\mathbf{a}_1$ direction [5]. The chiral angle for the axis of the so-called *zigzag* nanotube corresponds to $\theta = 0°$, while that for the so-called *armchair* nanotube axis corresponds to $\theta = 30°$, and the nanotube axis for the so-called chiral nanotubes corresponds to $0 < \theta < 30°$, as far as handedness [6] is not considered. The nanotube diameter d_t can be written in terms of the integers (n, m) as

$$d_t = C_h/\pi = \sqrt{3}a_{CC}(m^2 + mn + n^2)^{1/2}/\pi \ , \tag{2}$$

where a_{CC} is the nearest-neighbor C–C distance (1.421 Å in graphite), and C_h is the length of the chiral vector $\mathbf{C}_h$. The chiral angle θ is given by

$$\theta = \tan^{-1}\left[\sqrt{3}m/(m + 2n)\right] \ . \tag{3}$$

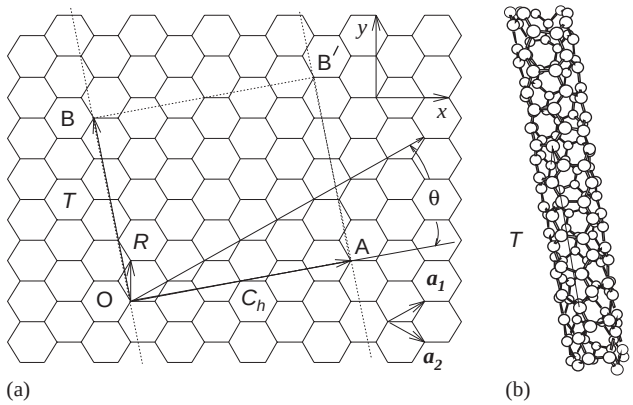

Fig. 1. (a) The unrolled honeycomb lattice of a nanotube. When we connect sites O and A, and sites B and B′, a portion of a graphene sheet can be rolled seamlessly to form a SWNT. The vectors OA and OB define the chiral vector $\mathbf{C}_h$ and the translational vector $\mathbf{T}$ of the nanotube, respectively. The rectangle OAB′B defines the unit cell for the nanotube. The figure is constructed for an $(n, m) = (4, 2)$ nanotube [1]. (b) The (4, 2) SWNTs, showing the translation vector $\mathbf{T}$.

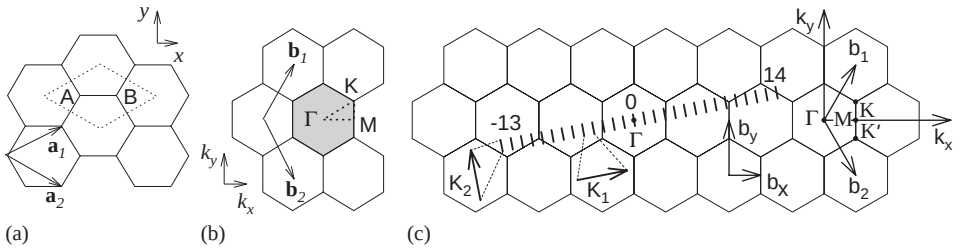

Fig. 2. (a) The unit cell (dotted rhombus), containing sites A and B where carbon atoms are located, and (b) the Brillouin zone (shaded hexagon) of a graphene or 2D graphite layer. $\mathbf{a}_i$ and $\mathbf{b}_i$ $(i = 1, 2)$ are basis vectors and reciprocal lattice vectors, respectively. The high symmetry points, Γ, K and M are indicated [7]. (c) Parallel equidistant lines represent the cutting lines for the (4, 2) nanotube, shown in Fig. 1. The cutting lines are labeled by the cutting line index μ, which assumes integer values from $1 - N/2 = -13$ to $N/2 = 14$.

Thus, a nanotube can be specified by either its (n, m) indices or equivalently by d_t and θ. Next we define the unit cell OBB′A of the 1D nanotube in terms of the unit cell of the 2D honeycomb lattice defined by the vectors $\mathbf{a}_1$ and $\mathbf{a}_2$ (Fig. 1).

In Fig. 2 we show (a) the unit cell in real space and (b) the Brillouin zone in reciprocal space of 2D graphite as a dotted rhombus and shaded hexagon, respectively, where $\mathbf{a}_1$ and $\mathbf{a}_2$ are basis vectors in real space, and $\mathbf{b}_1$ and $\mathbf{b}_2$ are reciprocal lattice basis vectors. In the x, y coordinate system shown in Fig. 2, the real space basis vectors $\mathbf{a}_1$ and $\mathbf{a}_2$ of the hexagonal lattice are expressed as $\mathbf{a}_1 = (\sqrt{3}a/2, a/2)$ and $\mathbf{a}_2 = (\sqrt{3}a/2, -a/2)$, where $a = |\mathbf{a}_1| = |\mathbf{a}_2| = 1.42 \times \sqrt{3} = 2.46\,\text{Å}$ is the lattice constant of a graphene or 2D graphite layer. Correspondingly, the basis vectors $\mathbf{b}_1$ and $\mathbf{b}_2$ of the reciprocal lattice are given by $\mathbf{b}_1 = (2\pi/\sqrt{3}a, 2\pi/a)$ and $\mathbf{b}_2 = (2\pi/\sqrt{3}a, -2\pi/a)$ corresponding to the graphene lattice constant of $4\pi/\sqrt{3}a$ in reciprocal space. The direction of the basis vectors $\mathbf{b}_1$ and $\mathbf{b}_2$ of the reciprocal hexagonal lattice are rotated by 30° from the basis vectors $\mathbf{a}_1$ and $\mathbf{a}_2$ of the hexagonal lattice in real space, as shown in Fig. 2. The three high symmetry points, Γ, K and M of the Brillouin zone are shown as the center, the corner, and the center of the edge, respectively, of the shaded hexagon that corresponds to the Brillouin zone of 2D graphite.

To define the unit cell for the 1D nanotube, we define the vector OB in Fig. 1 as the shortest repeat distance along the nanotube axis, thereby defining the translation vector $\mathbf{T}$

$$\mathbf{T} = t_1\mathbf{a}_1 + t_2\mathbf{a}_2 \equiv (t_1, t_2)\ , \tag{4}$$

where the coefficients t_1 and t_2 are related to (n, m) by

$$t_1 = (2m + n)/d_R, \quad t_2 = -(2n + m)/d_R\ , \tag{5}$$

where d_R is the greatest common divisor of $(2n + m, 2m + n)$ and is given by

$$d_R = \begin{cases} d & \text{if } n - m \text{ is not a multiple of } 3d\ , \\ 3d & \text{if } n - m \text{ is a multiple of } 3d \end{cases} \tag{6}$$

in which d is the greatest common divisor of (n, m). The magnitude of $\mathbf{T}$, the translation vector, is $|\mathbf{T}| = T = \sqrt{3}C_h/d_R$. The unit cell of the nanotube is defined as the area delineated by the vectors $\mathbf{T}$ and $\mathbf{C}_h$. The number of hexagons, N, contained within the 1D unit cell of a nanotube is determined by the

integers (n, m) and is given by

$$N = 2(m^2 + n^2 + nm)/d_R \ . \tag{7}$$

The addition of a single hexagon to the honeycomb structure in Fig. 1 corresponds to the addition of two carbon atoms. Assuming a value $a_{CC} = 0.142$ nm on a carbon nanotube, we obtain $d_t = 1.36$ nm and $N = 20$ for a (10,10) nanotube. Since the real-space unit cell is much larger than that for a 2D graphene sheet, the 1D Brillouin zone (BZ) for the nanotube is much smaller than the BZ for a graphene 2D unit cell. Because the local crystal structure of the nanotube is so close to that of a graphene sheet, and because the Brillouin zone is small, Brillouin zone-folding techniques have been commonly used to obtain approximate electron $E(k)$ and phonon $\omega(q)$ dispersion relations for carbon nanotubes with specific (n, m) geometrical structures.

Whereas the lattice vector $\mathbf{T}$, given by Eq. (4), and the chiral vector $\mathbf{C}_h$, given by Eq. (1), both determine the unit cell of the carbon nanotube in real space, the corresponding vectors in reciprocal space are the reciprocal lattice vectors $\mathbf{K}_2$ along the nanotube axis and $\mathbf{K}_1$ in the circumferential direction, which gives the discrete k values in the direction of the chiral vector $\mathbf{C}_h$. The vectors $\mathbf{K}_1$ and $\mathbf{K}_2$ are obtained from the relation $\mathbf{R}_i \cdot \mathbf{K}_j = 2\pi\delta_{ij}$, where $\mathbf{R}_i$ and $\mathbf{K}_j$ are, respectively, the lattice vectors in real and reciprocal space, and $\mathbf{K}_1$ and $\mathbf{K}_2$ therefore satisfy the relations

$$\mathbf{C}_h \cdot \mathbf{K}_1 = 2\pi, \quad \mathbf{T} \cdot \mathbf{K}_1 = 0, \quad \mathbf{C}_h \cdot \mathbf{K}_2 = 0, \quad \mathbf{T} \cdot \mathbf{K}_2 = 2\pi \ . \tag{8}$$

From Eqs. (8) it follows that $\mathbf{K}_1$ and $\mathbf{K}_2$ can be written as

$$\mathbf{K}_1 = \frac{1}{N}(-t_2\mathbf{b}_1 + t_1\mathbf{b}_2), \quad \mathbf{K}_2 = \frac{1}{N}(m\mathbf{b}_1 - n\mathbf{b}_2) \ , \tag{9}$$

where $\mathbf{b}_1$ and $\mathbf{b}_2$ are the reciprocal lattice vectors of a 2D graphene sheet [see Fig. 2(b)]. The N wave vectors $\mu\mathbf{K}_1$ ($\mu = 1 - N/2, \ldots, N/2$) give rise to N discrete k vectors or cutting lines [8] in the circumferential direction [see Fig. 2(c)]. For each of the μ discrete values of the circumferential wave vectors, 1D electronic energy bands appears (one π-band and one π^*-band), whereas each μ gives rise to 6 branches in the phonon dispersion relations. Because of the translational symmetry of $\mathbf{T}$, we have continuous wave vectors in the direction of $\mathbf{K}_2$ for a carbon nanotube of infinite length. However, for a nanotube of finite length L_t, the spacing between wave vectors is $2\pi/L_t$, and effects on the electronic structure associated with the finite nanotube length have been observed experimentally [9].

Chiral nanotubes are also described by their handedness, and can be either left or right handed. The definition is not unique from a symmetry point of view [6,8] for an unperturbed SWNT, and handedness effects can only be experimentally observed when externally applied fields, such as those associated with an incident laser beam or with an applied magnetic field, are used to break time reversal symmetry. The handedness can also be probed by scanning probe methods, but, in general, the handedness of a SWNT does not strongly affect its physical properties [6].

2.2. Electronic structure

To first order, the electronic structure of a carbon nanotube can be obtained from its parent material, 2D graphite, but in the case of SWNTs, the quantum confinement of the 1D electronic states must be taken into account. The electronic σ bands are responsible for the strong in-plane covalent bonds within the 2D graphene sheets, while the π bands are responsible for weak van der Waals interactions between

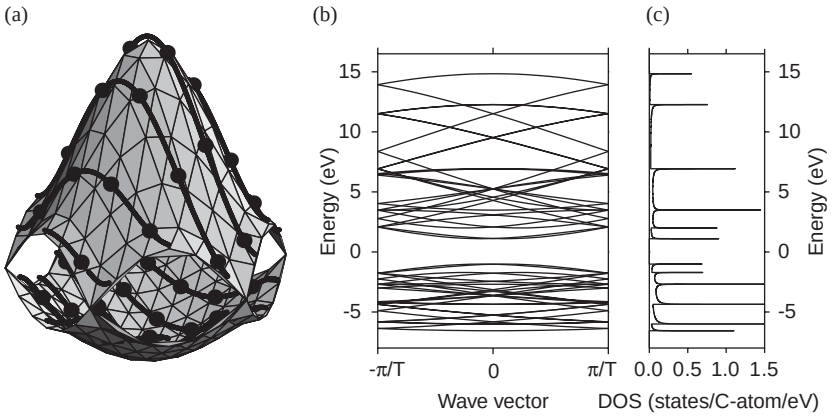

Fig. 3. (a) The calculated constant energy contours for the conduction and valence bands of a 2D graphene layer in the first Brillouin zone using the π-band nearest neighbor tight binding model [1]. The valence and conduction bands touch in the K points. Solid curves show the cutting lines for the (4, 2) nanotube [8], as shown in Fig. 2(c), but translated to the first Brillouin zone of 2D graphite, the dark points indicating the connection points. (b) Electronic energy band diagram for the (4, 2) nanotube obtained by zone-folding from (a). (c) Density of electronic states for the band diagram shown in (b).

such graphene sheets in 3D graphite. In contrast to the σ bands, the π bands are close to the Fermi level, so that electrons can be excited from the valence (π) to the conduction (π^*) band optically. Fig. 3(a) shows the electronic dispersion for the π and π^* bands of 2D graphite in the first Brillouin zone, obtained with the tight binding (TB) method [1]. The optical transitions occur close to the corners of the 2D hexagonal Brillouin zone, called the K points, where the valence and conduction bands touch each other [see Fig. 3(a)]. The energy dispersion around the K point is linear in k which is responsible for the unique solid-state properties of both 2D graphite and SWNTs.

The cutting lines of allowed wave vectors in the carbon nanotube reciprocal space can be represented in the 2D graphene sheet Brillouin zone, as shown in Fig. 3(a) [8], where all the cutting lines for the (4, 2) SWNT [see Fig. 2(c)] were translated to the first Brillouin zone of 2D graphite and joined at "connecting points" [see Fig. 3(a)]. The electronic band structure of the nanotube can be easily obtained, as shown in Fig. 3(b), by superimposing the 1D cutting lines on the 2D electronic constant energy surfaces. The SWNT electronic structures in Fig. 3(a) and (b) are given for a (4, 2) SWNT, that is chosen here for illustrative purposes. For such a small diameter SWNT, however, the large curvature of the graphene sheet induces changes in the C–C bond distances and causes a mixing of the σ and π bonds. Thus, more accurate methods than a nearest neighbor tight binding model must be used to describe the electronic structure for small diameter SWNTs [10].

Although the 1D electronic band structure of the small diameter tube, shown in Fig. 3(b), appears to be complex, it becomes simpler when considering the 1D density of electronic states, as shown in Fig. 3(c). It is of major significance that the optical absorption or emission rate in nanotubes is related primarily to the electronic states at the van Hove singularities (vHSs), thereby greatly simplifying the analysis of the optical experiments. The vHSs closer to the Fermi level originate from cutting lines closer to the K point in the 2D Brillouin zone.

SWNTs can be classified into three different classes, according to whether $\mathrm{MOD}(2n + m, 3) = 0, 1$ or 2, where the integers 0, 1, 2 denote the remainders when $(2n + m)$ is divided by 3 (see right panels in

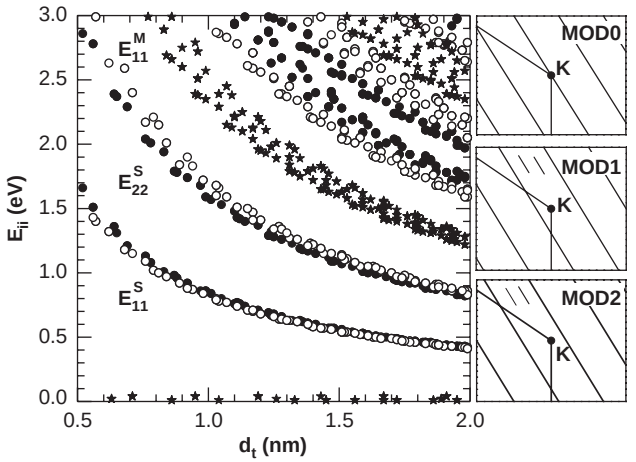

Fig. 4. The left panel shows the electronic transition energies E_{ii} vs. nanotube diameter d_t for SWNTs calculated by the first-neighbor tight binding method, with the transfer integral $\gamma_0 = 2.9\,\text{eV}$, the carbon–carbon distance $a_{\text{C–C}} = 0.142\,\text{nm}$, and neglecting nanotube curvature effects. Stars, filled and open circles stand for MOD0, MOD1 and MOD2 SWNTs, respectively [11]. The right panels show schematic figures defining the SWNT classes: MOD0—metallic, where one cutting line crosses the K point; MOD1 and MOD2—semiconducting, with an opposite chirality dependence for E_{ii}^{S}, as shown on the left panel, where it is, for example, seen that the energy levels for MOD1 semiconducting SWNTs E_{33}^{S} and E_{44}^{S} lie close to one another but MOD2 E_{33}^{S} and E_{44}^{S} lie far apart. The spread in the E_{ii} bands at constant diameter within this approximation is due to a trigonal warping effect (see text).

Fig. 4) [11]. Here MOD1 and MOD2 SWNTs are two types of semiconducting nanotubes, since no allowed k vector crosses the K point. For MOD0 SWNTs a cutting line crosses the K point and these SWNTs are classified as "metallic". However, due to the curvature effect, only armchair ($n = m$) SWNTs are truly metallic, while the other MOD0 SWNTs ($n \neq m$) are metallic at room temperature, but exhibit a small ($\sim$ meV) chirality-dependent energy gap (quasi-metallic) at lower temperatures.

The distance K_1 between two neighboring cutting lines in Figs. 2(c) and 3(a) is related to the nanotube diameter d_t by $K_1 = 2/d_t$, leading to a $1/d_t$ dependence for the distance between van Hove singularities (vHSs). The direction of the cutting lines relative to the axes of the hexagonal 2D Brillouin zone depends on the rolling up direction relative to the unit vector directions $\mathbf{a}_1$ and $\mathbf{a}_2$ of the 2D-graphite sheet. Thus the cutting line direction depends on the nanotube chiral angle θ, leading to a chirality dependence for the energies where the van Hove singularities occur, since the equi-energy contours around the K points are not circles, but rather exhibit a trigonally warped shape [1]. It is, therefore, easy to imagine that each (n, m) SWNT exhibits a different set of vHSs in its valence and conduction bands, and a different set of electronic transition energies for optical transitions between its valence and conduction band vHSs. For this reason, optical experiments can be used for the structural determination of a given (n, m) carbon nanotube.

By calling E_{ii} the electronic transition energies between the electronic valence and conduction bands with the same symmetry (see Section 4.2 for symmetry considerations), with the subscript $i = 1, 2, 3, \ldots$ labeling the E_{ii} values for a given SWNT as their energy magnitude increases [1], we see that the set of measured E_{ii} values will be specific to each individual (n, m) nanotube. Fig. 4 shows the E_{ii} values for all the (n, m) SWNTs with diameter between 0.5 and 2.0 nm, calculated using the tight binding method. This

so-called Kataura plot [12] has been widely used to interpret the optical spectra from carbon nanotubes. Superscripts S or M are used to denote the electronic transition energies E_{ii}^{M} for metallic SWNTs and E_{ii}^{S} for semiconducting SWNTs.

It is important to introduce the concept of the joint density of states (JDOS), that is pertinent to the optical processes. While the DOS is the density of electronic states vs. energy above and below the Fermi level, the JDOS is the density of electronic states that can absorb/emit photons as a function of the photon energy. Therefore, the JDOS starts from zero energy, and exhibits vHSs at energies equivalent to the energy difference between vHSs in the DOS, subject to optical selection rules. Fig. 4 plots the positions of the vHSs in the JDOS for many SWNTs, considering the selection rules for light polarized along the nanotube axis, as discussed in Section 4.2.

2.3. Phonon structure

Phonons denote the quantized normal mode vibrations that strongly affect many processes in condensed matter systems, including thermal, transport and mechanical properties. The 2D graphene sheet has two atoms per unit cell, thus having 6 phonon branches, as shown in Fig. 5(a). Since the SWNTs can be considered to be a 2D graphene sheet that has been rolled up seamlessly, a similar folding procedure, as was used for describing the electronic structure in Section 2.2, is generally applied to obtain the phonon dispersion relations and phonon density of states for SWNTs from those of the 2D graphene sheet [1]. The phonon dispersion for a (10,10) SWNT obtained by this folding procedure is illustrated in Fig. 5(c), and the respective phonon DOS is shown in Fig. 5(d). The large amount of sharp structure in the phonon density of states in Fig. 5(d) for the (10,10) SWNT reflects the many phonon branches and the 1D nature of SWNTs relative to 2D graphite arising from the quantum confinement of the phonon states into van Hove

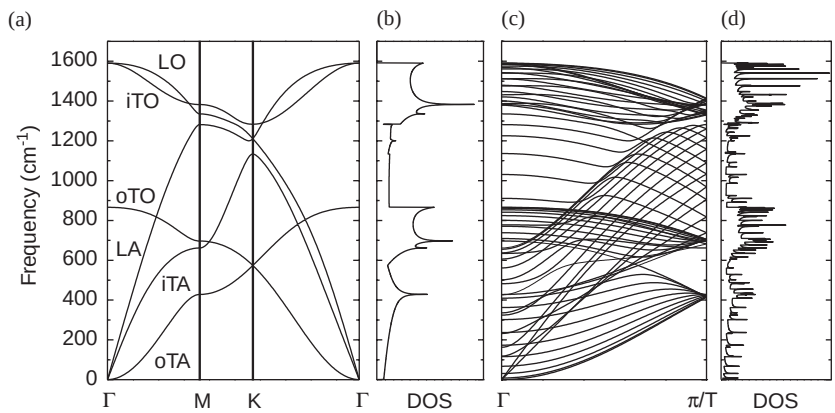

Fig. 5. (a) Phonon dispersion of 2D graphite using the force constants from [14]. The phonon branches are labeled: out-of-plane transverse acoustic (oTA); in-plane transverse acoustic (iTA); longitudinal acoustic (LA); out-of-plane transverse optic (oTO); in-plane transverse optic (iTO); longitudinal optic (LO). (b) The phonon density of states for a 2D graphene sheet. (c) The calculated phonon dispersion relations of an armchair carbon nanotube with $(n, m) = (10, 10)$, for which there are 120 degrees of freedom and 66 distinct phonon branches [1], calculated from (a) by using the zone folding procedure. (d) The corresponding phonon density of states for a (10,10) nanotube.

singularities. The phonon density of states for 2D graphite is shown in Fig. 5(b) for comparison. This 2D phonon DOS can be recovered by summing the 1D phonon density of states for many SWNTs [1,13].

Phonons play an important role as a carrier of thermal energy in thermal conduction processes and in thermodynamic properties, such as the heat capacity, and as an important scattering process for bringing electrons into equilibrium with the lattice in various electron transport phenomena, such as electrical conductivity, magneto-transport phenomena, and thermo-electricity. The vibrational spectra also determine the speed of sound, elastic properties of solids, and their mechanical properties. Phonons, through their interaction with electrons, can also mediate interactions and pairing between electrons, giving rise to superconductivity. These topics are particularly interesting in 1D systems, because of the van Hove singularities that 1D systems exhibit. These phenomena are even more interesting in SWNTs which allow these unique 1D effects to be studied in detail, since a 1D system blends the singular energy levels of molecules (delta functions in the DOS) with the quasi-continuous behavior of solid-state systems along the nanotube axis.

Besides the van Hove singularities in the phonon DOS, carbon nanotubes also exhibit some other unusual aspects regarding their phonon dispersion relations, such as four acoustic branches. In addition to the longitudinal acoustic and transverse acoustic modes, there are two acoustic twist modes for rigid rotation around the tube axis, which are important for heat transport and charge carrier scattering. Also important for coupling electrons to the lattice are the low-lying optical modes at the center of the Brillouin zone $q = 0$. These modes include one with E_2 symmetry expected at $\sim 17\,\mathrm{cm}^{-1}$ (the squash mode), one with E_1 symmetry, expected at $\sim 118\,\mathrm{cm}^{-1}$, and one with A symmetry (the radial breathing mode) expected at $\sim 165\,\mathrm{cm}^{-1}$ for a (10,10) SWNT [1]. Of these three low-energy phonon modes, it is only the radial breathing mode (RBM) with A symmetry, where all the carbon atoms are vibrating in phase in the radial direction, that has been studied experimentally. The most interesting details about the rich phonon structure of carbon nanotubes will be discussed in the next sections.

3. Classification of Raman scattering processes

In the Raman spectra of graphite and SWNTs, there are many features that can be identified with specific phonon modes and with specific Raman scattering processes that contribute to each feature. The Raman spectra of graphite and SWNTs can provide us with much information about the exceptional 1D properties of carbon materials, such as their phonon structure and their electronic structure, as well as information about sample imperfections (defects). Since mechanical properties, elastic properties and thermal properties also are strongly influenced by phonons, Raman spectra provide much general information about the structure and properties of SWNTs.

Raman scattering is the inelastic scattering of light. During a scattering event, (1) an electron is excited from the valence energy band to the conduction energy band by absorbing a photon, (2) the excited electron is scattered by emitting (or absorbing) phonons, and (3) the electron relaxes to the valence band by emitting a photon. We generally observe Raman spectra for the scattered photon (light) whose energy is smaller by the phonon energy than that of the incident photon. By measuring the intensity of the scattered light as a function of frequency downshift (losing energy) of the scattered light, which is what is plotted in Raman spectra, we obtain an accurate measure of the phonon frequencies of the material. By combining this information with the original geometrical structure of a crystal (or molecule), we can deduce a model for the phonon dispersion relations (or normal mode frequencies). Raman scattering can occur for phonon

emission (as described above) or by phonon absorption, and these two processes are called the Stokes process and anti-Stokes process, respectively. Since Raman scattering refers to the inelastic scattering of light, not only phonons, but any elementary excitation (such as a magnon, plasmon etc.) can be involved in a scattering process in which the elementary excitation satisfies energy–momentum conservation in the scattering process.

3.1. First-order Raman scattering in the G-band and RBM of SWNTs

The number of emitted phonons before relaxation of the lattice can be one, two, and so on, which we call, respectively, one-phonon, two-phonon and multi-phonon Raman processes. The order of a scattering event is defined as its number in the sequence of the total scattering events, including elastic scattering by an imperfection (such as a defect or edge) of the crystal. The lowest order process is the first-order Raman scattering process which gives Raman spectra involving one-phonon emission [see Fig. 6(a)]. A scattering event with only elastic scattering, i.e., change of photon direction but no frequency shift, corresponds to Rayleigh scattering of light. In order for an electron to recombine with a hole, the scattered $\mathbf{k}+\mathbf{q}$ states should not differ from $\mathbf{k}$ by more than two times the photon wave vector. This momentum conservation requirement and the small wave vector of the photon is the reason why we usually observe zone-center $\mathbf{q}=\mathbf{0}$ or Γ point phonon modes in a solid.

In 2D graphite, the so-called G band around $1582\,\mathrm{cm}^{-1}$ is the only first-order Raman peak [see Fig. 5(a)]. Another $\omega \neq 0$ phonon mode, the out-of-plane transverse optical phonon (oTO) mode, is not Raman active but is infrared active. In SWNTs, the G band spectra, which is split into many features around $1580\,\mathrm{cm}^{-1}$, and the lower frequency radial breathing mode (RBM) are usually the strongest features in SWNT Raman spectra, and are both first-order Raman modes. The RBM is a unique phonon mode, appearing only in carbon nanotubes and its observation in the Raman spectrum provides direct evidence that a sample contains SWNTs. The RBM is a bond-stretching out-of-plane phonon mode for which all the carbon atoms move coherently in the radial direction, and whose frequency ω_{RBM} is about 100–$500\,\mathrm{cm}^{-1}$. The RBM frequency is inversely proportional to the tube diameter and is expressed as

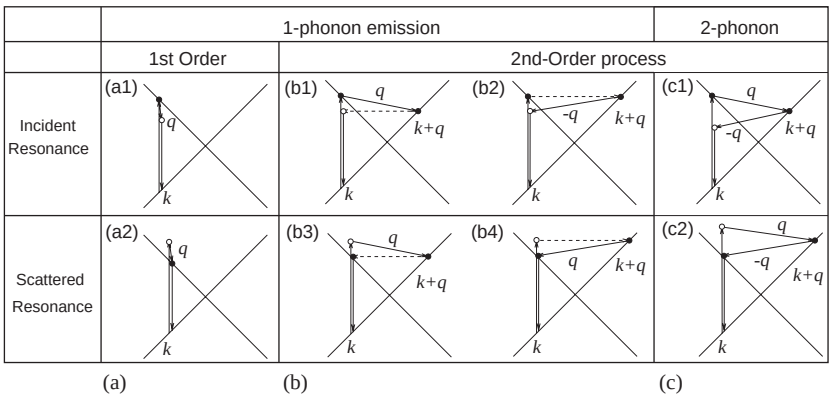

Fig. 6. (a) First-order and (b) one-phonon second-order, (c) two-phonon second-order, resonance Raman spectral processes. (top) incident photon resonance and (bottom) scattered photon resonance conditions. For one-phonon, second-order transitions, one of the two scattering events is an elastic scattering event (dashed lines). Resonance points are shown as solid circles. See text for details.

$\omega_{\mathrm{RBM}} = C/d_t$ (cm^{-1}) ($C = 248\,\mathrm{cm}^{-1}$ nm for isolated SWNTs on a SiO_2 substrate [3]). This dependence comes from the fact that the mass of all the carbon atoms along the circumferential direction is proportional to the diameter. It should be mentioned that several similar formulae have been proposed and a small correction to the formula comes from the effect of the substrate and from tube–tube interactions.

3.2. Resonance and non-resonance Raman scattering

When the optical absorption (or emission) is to (or from) a real electronic state, the energy denominators in the oscillator strength (see Section 4.1) becomes singular. This is a general resonance phenomenon that occurs in the presence of an oscillating external field. There are two resonance conditions for optical transitions: (1) resonance with the incident laser photon (incidence resonance) and (2) resonance with the scattered photon (scattered resonance). When the resonance occurs with the incident photon, the incident laser light has the same energy (E_{L}) as the energy separation between the two electronic states in resonance (ΔE), while the scattered photon has an additional energy of the phonon $\hbar\omega$,

$$E_{\mathrm{L}} = \Delta E \ \text{(incident resonance)} \ ,$$

$$E_{\mathrm{L}} = \Delta E + \hbar\omega \ \text{(scattered resonance)} \ . \tag{10}$$

Thus in the Stokes Raman process, the shift in the resonant energy for the scattered resonance state is larger than that for incident resonance state by the phonon energy. For the case of Raman scattering in SWNTs, the phonon energies of the *G*-band (0.2 eV) are sufficiently larger than that for the RBM (0.02 eV) when compared with the resonance energy width (10 meV), so that we can observe the RBM and *G*-band modes at the same time only for the incident resonance condition but not for the scattered resonance condition.

If the laser energy E_{L} does not coincide with the resonance energies on the right-hand side of Eq. (10), the optical transition in the Raman scattering process can be understood as a transition to a virtual state. The corresponding signal gives rise to what is called non-resonant Raman spectra which are much weaker in intensity than resonance Raman spectra. The resonance Raman process increases the signal by a factor of approximately 10^3 in comparison to the intensity for a non-resonance Raman process.

In the case of SWNTs, not only resonant enhancement but also a singularity in the JDOS contributes to the Raman intensity. When the laser energy of either the incident or the scattered light has the same energy as a vHS energy in the JDOS, the Raman intensity becomes extremely strong for any SWNT that satisfies the resonance condition. This is the reason why we can get a measurable signal from a single isolated SWNT in the presence of many non-resonant (n, m) SWNTs.

In order to understand resonance Raman scattering, theoretical calculations of the electronic and phonon structure, as discussed in Section 2, are needed. By specifying the resonance energy and phonon energy for a given SWNT, we can assign the Raman signal to specific (n, m) values and phonon modes. Group theory tells us that not all electronic states and not all phonon modes are relevant to the Raman process, depending on the symmetry of the (n, m) SWNT. For an optical transition (photon absorption and emission), dipole selection rules are needed to understand which transitions are allowed, and a second rank symmetrical tensor form is needed to describe the Raman-active modes. More strictly, we need to consider the symmetry of the electron–photon and electron–phonon matrix elements for a given solid. In Section 4, we discuss these subjects regarding the resonance Raman spectra for SWNTs.

3.3. Second-order Raman scattering, D- and G′-band

In second-order Raman scattering [see Fig. 6(b) and 6(c)], **q** and $-\mathbf{q}$ scattering wave vectors are involved, so that an electron can return to its original **k** position after scattering. Here bold font symbols are used to denote vectors, while the corresponding italic font is used to denote lengths of the vectors. Second-order Raman scattering consists of (1) two-phonon scattering events, or (2) one-phonon and one-elastic scattering event. In the case of two-phonon scattering events, we can have involvement of: (1a) the same phonon modes (overtone mode) or (1b) different phonon modes (combination modes).

In carbon materials, there are several weak Raman signals whose phonon frequencies change with changing laser excitation energy [15–19] which is called "dispersive" behavior. A typical example of this feature is the *D*-band at 1350 cm^{-1} whose frequency changes by 53 cm^{-1} as a result of changing the laser energy E_{L} by 1 eV. Double resonance (DR) Raman theory [20], as discussed in this section, works well for explaining the dispersive phonon modes in which a non-zone-center ($q \neq 0$) phonon mode and a second-order Raman process are relevant to these weak spectral features [18,19,21,22]. In principle, for solids, such a process is allowed for any two phonons were vectors q and $-q$, leading to background noise, unless special resonance requirements are fulfilled, as discussed below.

In second-order DR Raman processes for carbon materials [see Fig. 6(b)], the electron (1) absorbs a photon at a **k** state, (2) scatters to $\mathbf{k}+\mathbf{q}$ states, (3) scatters back to a **k** state, and (4) emits a photon by recombining with a hole at a **k** state. The two scattering processes consist of either elastic scattering by defects of the crystal or inelastic scattering by emitting a phonon, as shown in Fig. 6. Thus (1) one-elastic and one-inelastic scattering event [Fig. 6(b)] and (2) two-inelastic scattering events [Fig. 6(c)] are relevant to second-order Raman spectroscopy. Hereafter we call them, respectively, one- and two-phonon double-resonance Raman spectra [21].

As discussed in Section 2, the electronic structure of 2D graphite near the Fermi energy is linear in wave vector k, which is expressed by the crossed solid lines in Fig. 6. The crossing point corresponds to the Fermi energy located at the *K* point in the Brillouin zone. When the laser energy E_{L} increases, the resonance k vector for the electron moves away from the *K* point. In the DR process, the corresponding q vector for the phonon increases with increasing k, measured from the *K* point. Thus by changing the laser energy, we can observe the phonon energy $\hbar\omega(q)$ along the phonon dispersion relations (Fig. 5). This effect is observed experimentally as a dispersion of the phonon energy as a function of excitation laser energy E_{L} [21]. A tunable laser system can directly show this dispersive behavior of a dispersive feature in the Raman spectrum.

The initial (or final) k and the intermediate $k+q$ state exist on the equi-energy contour of the electronic structure.[1] An equi-energy contour of graphite is a circle around the *K* point in the 2D Brillouin zone. As a result, the possible q states are on circles which we rotate around Γ (or the *K* point). In this case, the density of states for possible q states becomes singular for $q=0$ and $2k$ [22,23]. Thus there are two double resonance peaks corresponding to the $q=0$ and $2k$ conditions. For the peak at $q=0$, the corresponding phonon frequency does not depend on laser energy.

In a DR Raman process, two resonance conditions for three intermediate states should be satisfied, in which the intermediate $\mathbf{k}+\mathbf{q}$ state is always a real electronic state and either the initial or the final **k** states is a real electronic state. As for one-phonon DR Raman spectroscopy [see Figs. 6(b1) and (b2)], the inelastic scattering process gives a shorter phonon **q** vector from the initial **k** state than the elastic

[1] Here we neglect the small phonon energy compared with a much larger electronic energy.

Table 1
Properties of the various Raman features in graphite and SWNTs[a]

Name[b]	ω (cm^{-1})	Res.[c]	dω/dE_L[d]	Notes[e]
iTA	288	DR1	129	iTA mode, intravalley scattering ($q = 2k$)
LA	453	DR1	216	LA mode, intravalley scattering ($q = 2k$)
RBM	$248/d_t$	SR	0	Nanotube only, vibration of radius
IFM$^-$	750	DR2	−220	Combination mode oTO–LA ($q = 2k$)[h]
oTO	860	DR1	0	IR-active mode in graphite
IFM$^+$	960	DR2	180	Combination mode oTO + LA ($q = 2k$)[h]
D	1350	DR1	53	LO or iTO mode, intervalley scattering ($q = 2k$)
LO	1450	DR1	0	LO mode, intervalley scattering ($q = 0$)
BWF[f]	1550	SR	0	Plasmon mode, only metallic carbons
G	1582	SR	0	Raman active mode of graphite[g]
M^-	1732	DR2	−26	overtone of oTO mode ($q = 2k$)
M^+	1755	DR2	0	overtone of oTO mode ($q = 0$)
iTOLA	1950	DR2	230	combination mode of iTO and LA
G′	2700	DR2	106	overtone of D mode
2LO	2900	DR2	0	overtone of LO mode
2G	3180	DR2	0	overtone of G mode

[a]Mode frequencies for dispersive modes are given at $E_L = 2.41$ eV.
[b]See Fig. 5 and Section 5 for an explanation of names.
[c]The following notation is used to classify the Raman scattering process: SR: first order; DR1: one-phonon double resonance; DR2; two-phonons double resonance.
[d]dω/dE_L denotes the change of the phonon frequency in cm^{-1} produced by changing the laser energy by 1 eV.
[e]Double resonance (DR) features are classified as intervalley and intravalley scattering processes (see Section 3.4).
[f]The Breit–Wigner–Fano lineshape is discussed in Section 3.6.
[g]G-band for graphite is at 1582 cm^{-1}. For SWNTs, there is a G^+ feature at 1590 cm^{-1} due to in-plane vibrations along the tube axis, and a diameter-dependent G^- feature at 1570 cm^{-1} for in-plane vibrations along the circumferential direction (see Section 6.2.1).
[h]The physics of the intermediate frequency modes (IFM) between 600–1100 cm^{-1} is interesting and complex, as discussed in Section 7.7.

scattering process in order to satisfy energy-momentum conservation. Both in graphite and in SWNTs, the D-band at 1350 cm^{-1} and the G'-band at 2700 cm^{-1} (for $E_L = 2.41$ eV) are, respectively, due to one- and two-phonon, second-order Raman scattering processes. Thus for graphite, the D-band spectra appearing at 1350 cm^{-1} (one-phonon DR) can be fitted to two Lorentzians, while the G'-band feature at 2700 cm^{-1} (two-phonon DR) can be fitted to one Lorentzian [23].

Typically the D-band and G'-band phonon frequencies would be measured for a laser energy of 2.41 eV and its dispersion would be 53 and 106 cm^{-1} eV^{-1}, respectively for the D-band and the G'-band for SWNTs. Many weak features in the Raman spectra for SWNTs can be assigned to one-phonon or two-phonon, second-order double resonance processes, and these are listed in Table 1.

3.4. Intravalley or intervalley DR Raman scattering

Since the phonon energy is much smaller than the relevant energy of the photo-excited electron, we can assume as a first approximation that an electron scatters from one k point to another k point on an

equi-energy line. In the case of graphite, there are two equi-energy circles around the K and K' points (two inequivalent hexagonal corners of the BZ). Thus we expect either a phonon scattering event in the vicinity of the K (or K') points or a scattering event that takes an electron from the K to K' points (or from K' to K), which we call intravalley or intervalley scattering, respectively.

In the first-order Raman process, since $q \sim 0$ is required, only intravalley scattering is possible. In the second-order Raman process, however, both intravalley and intervalley scattering are possible. In the case of intervalley scattering, the corresponding phonon vector is around the K point if the **q** vector is measured from the Γ point. When we consider the assignment to a two-phonon, second-order Raman scattering process, combination modes of one intra-valley and one inter-valley phonon are not possible, since in this case the **q** values would be different.

3.5. Stokes or anti-stokes Raman scattering

The scattering of an electron by a phonon consists of the emission of a phonon (Stokes shift) and the absorption of a phonon (anti-Stokes shift), which appear in the Raman spectra, respectively, on the smaller and larger energy sides of the incident laser energy. In a two-phonon process, we can generally expect a two-phonon absorption or a two-phonon emission process. Another possibility for a two-phonon scattering process could be a combination mode of a phonon absorption process and a phonon emission process.

The phonon involved in the absorption process should already be thermally excited. The number of μth phonon modes with wave vector q at a temperature T is given by the Bose–Einstein statistics.

$$n(q,\mu) = \frac{1}{\exp(\hbar\omega(q,\mu)/k_{\mathrm{B}}T) - 1} \ , \tag{11}$$

where k_{B} is the Boltzmann constant. Thus the anti-Stokes signal intensity decreases with decreasing temperature compared with the phonon energy scaled by k_{B} since $n(q,\mu) \sim \exp(-\hbar\omega(q,\mu)/k_{\mathrm{B}}T)$ for low temperatures ($k_{\mathrm{B}}T \ll \hbar\omega$). In non-resonant and in most resonant Raman scattering events, the relative spectral intensities for the Stokes and anti-Stokes processes reflect the temperature dependence of the relative phonon populations. In nanotube systems, where the JDOS has sharp van Hove singularities, the Stokes/anti-Stokes ratio is very sensitive to the resonance condition. This topic is further discussed in Section 6.1.2.

3.6. Breit–Wigner–Fano lineshape

The G-band of graphite intercalation compounds (GICs), and the G^--band feature in the Raman spectra of metallic SWNTs do not have a symmetric lineshape and can be fitted to a so-called Breit–Wigner–Fano (BWF) lineshape as follows:

$$I(\omega) = I_0 \frac{[1 + (\omega - \omega_{\mathrm{BWF}})/q\Gamma]^2}{1 + [(\omega - \omega_{\mathrm{BWF}})/\Gamma]^2} \ , \tag{12}$$

in which $1/q$ represents the asymmetry of the shape (interaction), while, ω_{BWF}, I_0 and Γ are fitting parameters of the central frequency, the intensity and the broadening factor, respectively. The BWF signal appears only when the electronic density of states at the Fermi energy $D(E_{\mathrm{F}})$ has a finite value. Thus we

observe a BWF lineshape only in metallic SWNTs, donor or accepter GICs, but not in semiconducting SWNTs or in graphite.

The BWF spectral shape occurs when a discrete energy excitation level interacts with a continuum of energy excitations, causing a resonance and anti-resonance effect $(1/q)$, and thus giving rise to a non-symmetric spectral lineshape for the discrete state. Depending on the strength of the interaction, both the peak position and the width of the spectral line are changed, with the asymmetry depending on whether the continuum of states is centered above or below the discrete state in energy. In the case of graphite and SWNTs, since the interaction with continuous states depends on the density of states at the Fermi energy, we consider the origin of the continuum spectra to be a low-energy plasmon.

3.7. Summary of phonon mode classifications

In summary, phonon spectra are classified by: (1) phonon modes that are involved, (2) first order or second order, (3) Stokes or anti-Stokes, (4) resonant or non-resonant, Raman scattering. For resonance Raman scattering (RRS), there are (5) incident laser resonance and scattered laser resonance conditions. For a second-order Raman process, we can further specify phonons by a (6) one-phonon or two-phonon, (7) intravalley or intervalley, or (8) $q = 0$ or $2k$, singular scattering process. In addition, for two-phonon scattering, there are (9) overtone or combination phonon modes. The resonance condition for the wave vector for first order and second order is, respectively, $\mathbf{q} \sim 0$ and ($\mathbf{q}$ and $-\mathbf{q}$). The resonance condition for the energy is (a) $E_{\mathrm{L}} = \Delta E$ for the incident resonance with the incident photon for all cases, while (b) $E_{\mathrm{L}} = \Delta E \pm E_{\mathrm{ph}}$ applies for the one-phonon scattered resonance condition (+ Stokes, − anti-Stokes) and (c) $E_{\mathrm{L}} = \Delta E \pm 2E_{\mathrm{ph}}$ for the two-phonon scattered resonance condition (see Section 3.2).

Using both experimental information and theoretical calculations, we summarize in Table 1 the mode frequencies, the classification of the pertinent scattering process and the frequency dispersion with variation of the laser energy E_{L} for all features appearing in the Raman spectra for graphite and SWNTs up to $3200\,\mathrm{cm}^{-1}$.

4. Resonance Raman intensity calculations

In this section, we discuss how to calculate the resonance Raman intensity. As discussed in Section 3, all Raman scattering events are a combination of two electron–photon interactions (absorption and emission) and either one or more electron–phonon interactions (phonon scattering), depending on whether the feature is associated with a one-phonon or a multi-phonon Raman process, respectively. In the case of a second-order one-phonon process, we must explicitly consider the electron-defect interaction (elastic scattering) for energy-momentum conservation. However, this scattering event depends sensitively on the detailed structure of the defect. Thus, we here consider only first-order one-phonon and second-order two-phonon interactions for simplicity. Moreover, hereafter in this section, we will consider only the calculation for the Stokes Raman intensity. When we consider the anti-Stokes Raman intensity, we change the sign of the phonon energy from $\hbar\omega$ to $-\hbar\omega$, and we take into account the number of thermally excited phonons for each phonon mode by using the Bose–Einstein distribution.

In describing how to calculate the Raman intensity for a resonance Raman process, a general formulation is presented in Section 4.1, and the selection rules that apply for Raman scattering in SWNTs are then developed (Section 4.2). Finally, in Sections 4.3 and 4.4 the unusual dependences of the scattering

intensity on nanotube diameter, chiral angle and laser excitation energy arising from the electron–photon and electron–phonon matrix elements are presented.

Although excitonic binding between the photoexcited electron and hole as well as many body electron–electron repulsion effects are known to be important for the precise calculation of the energies and intensities of specific resonance Raman and photoluminescence processes, these many body effects are not discussed in this paper for two reasons. Firstly it is easier to understand the selection rules for the unbound electron and hole, and secondly, it is expected that the general behaviors predicted by the band model and described below will not be strongly modified by an exciton-based many body model, once such calculations become available. Furthermore, the E_{11}^S levels will experience a strong exciton effect, although resonance Raman experiments are usually performed for exciton energies larger than E_{22}, where the exciton effect will give only small corrections to the transition energy.

4.1. Formulation of the Raman intensity

The first-order Raman intensity [see Fig. 6(a)] as a function of phonon energy, $\hbar\omega$, and of the incident laser energy, E_{L} is calculated by [20,24]

$$I(\omega, E_{\mathrm{L}}) = C\left(\frac{E_a}{E_j}\right)[n(q,\mu)+1]\sum_j \left|\sum_a \frac{M^{\mathrm{d}}(\mathbf{k}-\mathbf{q}, jb)M^{\mathrm{ep}}(\mathbf{q}, ba)M^{\mathrm{d}}(\mathbf{k}, aj)}{\Delta E_{aj}(\Delta E_{aj}-\hbar\omega)}\right|^2, \tag{13}$$

in which C is a constant independent of (n, m), the number of phonons $n(q, \mu)$ is given by Eq. (11) while $\Delta E_{aj} \equiv E_L - (E_a - E_j) - i\gamma$, and j, a and b denote, respectively, the initial state, the excited states, and the scattered state of an electron, while γ denotes the broadening factor of the resonance event. An electron at wave vector $\mathbf{k}$ is (1) excited by an electric dipole interaction $M^{\mathrm{d}}(\mathbf{k}, aj)$ with the incident photon to make a transition from j to a, and is then (2) scattered by emitting a phonon with phonon wave vector $\mathbf{q}$ by an electron–phonon interaction, $M^{\mathrm{ep}}(\mathbf{q}, ba)$, and (3) finally the electron emits a photon by an electric dipole transition, through the interaction $M^{\mathrm{d}}(\mathbf{k}-\mathbf{q}, jb)$. For an energy separation E_{aj} between the j and a states, the resonance conditions are either with the incident photon, $E_{\mathrm{L}} = E_{aj}$, or with the scattered photon, $E_{\mathrm{L}} = E_{aj} + \hbar\omega$. The sum in Eq. (13) is taken over all possible intermediate states specified by a and the initial states j. In order to take the sum for the intermediate states, we need to know the electric dipole matrix elements of the electron–photon interaction, M^{d}, and electron–phonon interaction, M^{ep}, which are given below in Sections 4.3 and 4.4, respectively. In the scattering process, energy-momentum conservation for an electron and phonon holds, but this is not explicitly written in Eq. (13).

The second-order, two-phonon Raman intensity (see Fig. 6) as a function of E_{L} and the sum of the two-phonon energies $\omega = \omega_1 + \omega_2$ is given by a similar formula

$$I(\omega, E_{\mathrm{L}}) = \sum_j \left|\sum_{a,b,\omega_1,\omega_2} J_{a,b}(\omega_1, \omega_2)\right|^2, \tag{14}$$

where

$$J_{a,b}(\omega_1, \omega_2) = \frac{M^{\mathrm{d}}(\mathbf{k}, jc)M^{\mathrm{ep}}(-\mathbf{q}, cb)M^{\mathrm{ep}}(\mathbf{q}, ba)M^{\mathrm{d}}(\mathbf{k}, aj)}{\Delta E_{aj}(\Delta E_{bj}-\hbar\omega_1)(\Delta E_{aj}-\hbar\omega_1-\hbar\omega_2)}. \tag{15}$$

Now we have two-phonon scattering processes with phonon wave vectors $\mathbf{q}$ and $-\mathbf{q}$. In order to get two resonance conditions at the same time, an intermediate electronic state E_{bj} is always in resonance ($E_{\mathrm{L}} = E_{bj} + \hbar\omega_1$), and either the incident resonance condition ($E_{\mathrm{L}} = E_{aj}$) or the scattered resonance condition ($E_{\mathrm{L}} = E_{aj} + \hbar\omega_1 + \hbar\omega_2$) is satisfied. For a second-order process, the one-phonon Raman intensity is calculated by replacing one of the two phonon scattering processes by an elastic impurity scattering process. Another point to mention is the energy uncertainty of γ in ΔE_j.

4.2. Selection rules for Raman scattering

The selection rules for the Raman spectra for SWNTs are quite special but follow from general group theoretical considerations.[2] We have several selection rules for different geometries for observation of resonance Raman scattering. To discuss the selection rules for the first-order (one phonon) Raman scattering process, we consider here the most general symmetry for a chiral SWNT (C_N symmetry) [17].

4.2.1. Symmetry of electron and phonon wavefunctions

Electron and phonon eigenfunctions of a SWNT are characterized by their 1D wave vectors (k for electrons and q for phonons) and by the cutting line index μ which specifies their symmetries. The symmetry is related to the number of nodes for their wavefunctions around the circumferential direction. The totally symmetric A electrons and phonons have no nodes ($\mu = 0$), while the wavefunctions with higher harmonics (E_μ) with $\mu \neq 0$, are doubly degenerate[3] and behave like $\sin(\mu\theta)$ and $\cos(\mu\theta)$. Thus the E_μ eigenfunctions have 2, 4, 6, ... nodes for $\mu = 1, 2, 3, \ldots$, respectively.

4.2.2. Geometry of Raman observations

In considering selection rules, we first put a SWNT in the direction of the z-axis. We can take two symmetric propagation directions (y and z) of light with respect to the SWNT. For a y-propagating photon, the two polarization directions, z and x are *inequivalent* relative to the nanotube axis, while for a z-propagating photon, the two polarization directions, x and y are *equivalent*.

The geometry of the Raman observation is usually expressed by four vectors

$$\mathbf{P}_{\mathrm{g}}[\mathbf{P}_{\mathrm{i}}, \mathbf{P}_{\mathrm{s}}]\mathbf{P}_{\mathrm{o}}, \quad (\mathbf{P} = X, Y, Z) \ , \tag{16}$$

where $\mathbf{P}_{\mathrm{g}}$ and $\mathbf{P}_{\mathrm{o}}$ are, respectively, the propagating directions of the incident and scattered light, and $\mathbf{P}_{\mathrm{i}}$ and $\mathbf{P}_{\mathrm{s}}$ are the polarization directions of the electric field of the incident and scattered light, respectively. We usually observe the Raman signal for the propagating direction y and the backscattered geometry ($Y[\mathbf{P}_{\mathrm{i}}, \mathbf{P}_{\mathrm{s}}]\bar{Y}$). For an isolated SWNT (or an aligned SWNT bundle), we can change the polarization of light relative to the SWNT axis, to select specific symmetry-allowed phonon modes.

4.2.3. Selection rules for optical transitions

Next we consider the selection rules for optical transitions. Depending on the polarization direction of light, the final electronic state is specified by the effect of the selection rule on a given initial state. To analyze the electron–photon processes, we search for vector-like basis functions. When inversion

[2] In order to understand this subsection, general knowledge from group theory is needed. If the reader is not familiar with group theory, the pertinent results can be obtained directly from Table 2.

[3] A and E_μ are labels of irreducible representations of the C_N group [1].

symmetry is present, the z basis function belongs to the A_u ($\mu = N/2$) irreducible representation where N is given by Eq. (7), while the x, y basis functions belong to E_{1u}. However, if there is no inversion symmetry (which would be the case for a general chiral nanotube), the z basis functions transform as the A irreducible representation while the (x, y) basis functions transform as E_1. Thus modes transforming as z and (x, y) can be observed in both the Raman and infrared spectra. Thus, using the dipole approximation for optical transitions, the corresponding dipole selection rule for an optical transition between SWNT sub-bands in the valence and conduction bands is given by $E_\mu^{\mathrm{v}} \rightarrow E_{\mu'}^{\mathrm{c}}$ with $(\mu' = \mu)$ for light polarized along Z, and with $(\mu' = \mu \pm 1)$ for light polarized along X [1,17,25].

4.2.4. Selection rules of first-order Raman processes

The Raman-active phonon modes belong to the irreducible representations with quadratic basis functions, i.e., $A(zz, xx + yy)$, $E_1(zx, xz)$, and $E_2(xx - yy, xy)$ which correspond to phonon wavefunctions with $\mu = 0, 1, 2$, respectively (see Section 4.2.1). Although SWNTs have a large number of phonon branches [see Fig. 5(c)], only A, E_1 and E_2 symmetry modes are Raman active in a first-order process.

For the $Y[\mathbf{P}_{\mathrm{i}}, \mathbf{P}_{\mathrm{s}}]\bar{Y}$ geometry, the total function obtained by multiplying the x, y, z of $\mathbf{P}_{\mathrm{i}}$ and $\mathbf{P}_{\mathrm{s}}$ with the quadratic phonon basis functions must be an even function of x, y, z. Otherwise an integration over space would give zero. The totally symmetric A modes are observed for incident and scattered light, polarized in the same direction ($Y[ZZ]\bar{Y}$ or $Y[XX]\bar{Y}$); E_1 modes for the cross-polarized direction ($Y[XZ]\bar{Y}$, $Y[ZX]\bar{Y}$), and E_2 modes for the incident (x) and scattered (x) light, polarized perpendicular to the nanotube axis ($Y[XX]\bar{Y}$), as summarized in Table 2 [25].

Table 2
Selection rules for the Raman backscattering processes in SWNTs (see text)

Process[a]	Geometry[b]	Phonon symmetry	Optical transition[c]
First order	$Y(ZZ)\bar{Y}$	A	$E_\mu \rightarrow E_\mu$
	$Y(XX)\bar{Y}$	A	$E_\mu \rightarrow E_{\mu\pm2}$
	$Y(XX)\bar{Y}$	E_2	$E_\mu \rightarrow E_\mu$
	$Y(XZ)\bar{Y}$[d]	E_1	$E_\mu \rightarrow E_{\mu\pm1}$
	$Z(XX)\bar{Z}$[e]	A	$E_\mu \rightarrow E_\mu$
	$Z(XY)\bar{Z}$[d]	E_2	$E_\mu \rightarrow E_{\mu\pm_2}$
Second order	$Y(ZZ)\bar{Y}$	$E_\mu + E_\mu$	$E_{\mu'} \rightarrow E_{\mu'}$
	$Y(XX)\bar{Y}$	$E_\mu + E_\mu$	$E_{\mu'} \rightarrow E_{\mu'}$
	$Y(ZX)\bar{Y}$[d]	$E_\mu + E_{\mu\pm1}$	$E_{\mu'} \rightarrow E_{\mu'\pm1}$
	$Y(XX)\bar{Y}$	$E_\mu + E_{\mu\pm2}$	$E_{\mu'} \rightarrow E_{\mu'\pm2}$
	$Z(XX)\bar{Z}$[e]	$E_\mu + E_\mu$	$E_{\mu'} \rightarrow E_{\mu'}$
	$Z(XY)\bar{Z}$[d]	$E_\mu + E_\mu \pm 2$	$E_{\mu'} \rightarrow E_{\mu'\pm2}$

[a] For the second-order processes, only two-phonon processes are considered. Selection rules for defect scattering need determination of the relevant defect structure.

[b] We consider z as the nanotube axis direction, and use the following notation for the scattering geometry: letters outside (inside) the parentheses indicate incident and scattered light propagation (polarization) directions. The symbols $\bar{Y}$ and $\bar{Z}$ are used in the table to denote back scattering.

[c] Here the electronic transition induced by the phonon scattering is indicated by the symmetry of the electronic states.

[d] For cross-polarized scattering, the same selection rule applies for symmetric processes, e.g., (ZX) and (XZ).

[e] For light propagating along the nanotube axis (Z), the same selection rules apply for (XX) and (YY) polarization geometries.

By combining the selection rules for the scattering geometry (Section 4.2.2) and for dipole-allowed optical transitions (Section 4.2.3) we can specify the selection rules for a symmetry-allowed first-order Raman process for a SWNT. For the electron–phonon interaction, phonons can scatter electrons from one cutting line μ to another μ', depending on the phonon symmetries, but subject to $\Delta\mu = \mu - \mu'$ (angular momentum conservation). For A phonon mode symmetry, we have $\Delta\mu = 0$, and for E_j phonon mode symmetries, $\Delta\mu = \pm j$. Combining the electron–incident photon, the electron–phonon, and the electron–scattered photon processes in proper sequence from a symmetry standpoint, yields the following possible Raman processes in SWNTs [8,26]:

$$
\begin{aligned}
&E_\mu^{\mathrm{v}} \xrightarrow{\parallel} E_\mu^{\mathrm{c}} \xrightarrow{A(ZZ)} E_\mu^{\mathrm{c}} \xrightarrow{\parallel} E_\mu^{\mathrm{v}}\\
&E_\mu^{\mathrm{v}} \xrightarrow{\perp} E_{\mu\pm1}^{\mathrm{c}} \xrightarrow{A(XX)} E_{\mu\pm1}^{\mathrm{c}} \xrightarrow{\perp} E_\mu^{\mathrm{v}}\\
&E_\mu^{\mathrm{v}} \xrightarrow{\parallel} E_\mu^{\mathrm{c}} \xrightarrow{E_1(ZX)} E_{\mu\pm1}^{\mathrm{c}} \xrightarrow{\perp} E_\mu^{\mathrm{v}}\\
&E_\mu^{\mathrm{v}} \xrightarrow{\perp} E_{\mu\pm1}^{\mathrm{c}} \xrightarrow{E_1(XZ)} E_\mu^{\mathrm{c}} \xrightarrow{\parallel} E_\mu^{\mathrm{v}}\\
&E_\mu^{\mathrm{v}} \xrightarrow{\perp} E_{\mu\pm1}^{\mathrm{c}} \xrightarrow{E_2(XX)} E_{\mu\mp1}^{\mathrm{c}} \xrightarrow{\perp} E_\mu^{\mathrm{v}}
\end{aligned}
\tag{17}
$$

consistent with the symmetries for the Raman-active modes A $(zz, xx+yy)$, E_1 (zx, xz), and E_2 $(xx-yy, xy)$, and with the basis functions for each irreducible representation, given between parenthesis.

Therefore, considering that the first-order Raman signal from isolated SWNTs can only be seen when in resonance with vHSs, these selection rules imply that for isolated SWNTs: (1) A modes can be observed for the (ZZ) scattering geometry for resonance with $E_{\mu\mu}$ vHSs, and for the (XX) scattering geometry for resonance with $E_{\mu,\mu\pm1}$ vHSs (the letters between parenthesis denote, respectively, the polarization direction for the incident and scattered light); (2) E_1 modes can be observed for the (ZX) scattering geometry for resonance of the incident photon with $E_{\mu\mu}$ vHSs, or for resonance of the scattered photon with $E_{\mu,\mu\pm1}$ vHSs, and for the (XZ) scattering geometry for resonance of the incident photon with $E_{\mu,\mu\pm1}$ vHSs, or for resonance of the scattered photon with $E_{\mu\mu}$ vHSs; (3) E_2 modes can only be observed for the (XX) scattering geometry for resonance with $E_{\mu,\mu\pm1}$ vHSs [8,26].

The absorption/emission of light parallel to the nanotube axis gives rise to van Hove singularities (vHSs) in the joint density of states (JDOS) here labeled E_{ii}, and these E_{ii} are shown in Fig. 4. This type of transition accounts for most of the observed optical spectra for SWNTs, indicating that the strong anisotropy of the optical absorption and emission of SWNTs is analogous to that found in a common dipole antenna.

4.2.5. Circularly polarized light and light polarized normal to tube axis

Interesting information can be obtained using circularly polarized light ($Z[X+iY, X+iY]\bar{Z}$, $Z[X-iY, X-iY]\bar{Z}$, $Z[X+iY, X-iY]\bar{Z}$),[4] or using light polarized normal to the tube axis, e.g., $(Y[XX]\bar{Y})$.

For light that is polarized perpendicular to the tube axis, only transitions between E_μ symmetry valence and $E_{\mu\pm1}$ symmetry conduction sub-bands (involving neighboring cutting lines in reciprocal space, as

[4] Circularly polarized light is obtained by light with X polarization and Y polarization components and a $\pi/2$ phase difference between them.

shown in Fig. 3) are dipole allowed [27]. Since there should be a band asymmetry with respect to the Fermi level,[5] the $E_\mu \leftrightarrow E_{\mu+1}$ transition energy would be different from the $E_{\mu-1} \leftrightarrow E_\mu$ energy, and the resulting energy differences would give a band asymmetry relative to the Fermi level. Circularly polarized light propagating along the SWNT axis direction could also be used to probe the chirality handedness (left and right) of the carbon nanotubes, since either $E_\mu \leftrightarrow E_{\mu+1}$ or $E_\mu \leftrightarrow E_{\mu-1}$ optical transitions occur, depending on the polarization of the light and the handedness of the SWNT [6]. Although experiments with circularly polarized light propagating along the nanotube axis directions and with light polarized normal to the nanotube axis and propagating normal to both of these directions are technically challenging, the experimental observation of E_2 symmetry modes in the Raman experiments provided the first evidence for the observation of $E_\mu \leftrightarrow E_{\mu\pm1}$ transitions [26].

4.2.6. Selection rules for combination modes

The combination mode (or overtone for the special case $\mu=\mu'$) will be Raman active if the direct product $\Gamma_\mu \bigotimes \Gamma_{\mu'}$ for the symmetries of nodes μ and μ' contains an irreducible representation $\Gamma_{\mu''}$ that is Raman active. Since any overtone $E_\mu \bigotimes E_\mu$ contains the totally symmetric A irreducible representation, a signal from any overtone of E_μ phonons can be observed in the (ZZ) or (XX) Raman scattering geometries. The symmetries $E_\mu \bigotimes E_{\mu\pm1}$ can be observed in the (ZX) and (XZ) scattering geometries, while $E_\mu \bigotimes E_{\mu\pm2}$ is active for the (XX) scattering geometry. For a defect-induced double resonance process, analysis of specific defects is necessary. For example, a point defect (e.g., vacancy) is localized in real space but delocalized in reciprocal space, so that a process with any symmetry type would be possible for this case. For combination modes with different Γ_μ and $\Gamma_{\mu'}$ symmetries, the Raman-active symmetries contained in the direct product $\Gamma_\mu \bigotimes \Gamma_{\mu'}$ must be explicitly considered.

The selection rules for several Raman processes in SWNTs are summarized in Table 2 [26–28].

4.3. Electron–photon matrix elements

In the photo-luminescence and photo-absorption processes, the optical intensities are given by the product of the electron–photon matrix element and density of states for the initial and the final states. In the case of carbon nanotubes, a vHS is essential for describing the optical processes and for assigning the observed absorption (emission) energy (see Section 3.2). However, some of the vHSs do not contribute to the photo-absorption signal because of the vanishing of their matrix elements [29,30]. For high symmetry points in the Brillouin zone, the vanishing matrix element can be understood by the selection rule as discussed in Section 4.2. However, when we discuss the k dependence of the intensity (in Section 4.1), we need to calculate the matrix element for the optical transition $M^{\mathrm{d}}(\mathbf{k})$ which is k dependent. In this section we show calculated results for the electron–photon matrix element within the tight binding formulation.

The absorption and spontaneous emission of light can be treated as an optical dipole transition matrix element at wave vector $(\mathbf{k})$ which has the form of an inner product of the polarization vector, $\mathbf{P}$, and the dipole vector, $\langle \Psi^{\mathrm{c}}(\mathbf{k})|\nabla|\Psi^{\mathrm{v}}(\mathbf{k})\rangle$ [29]

$$M^{\mathrm{d}}(\mathbf{k}) = i\frac{e\hbar}{m\omega}\sqrt{\frac{I}{\varepsilon c}}\mathrm{e}^{\mathrm{i}(\omega_f-\omega_i-\omega)t}\,\mathbf{P}\cdot\langle\Psi^{\mathrm{c}}(\mathbf{k})|\nabla|\Psi^{\mathrm{v}}(\mathbf{k})\rangle\ , \tag{18}$$

[5] The energy band width of the conduction band is expected to be larger than that of the valence band.

where I, ω, and $\mathbf{P}$ are the intensity, frequency, and polarization vector of the light, respectively, and $\Psi^i(\mathbf{k})$, $i = \mathrm{c}, \mathrm{v}$ are eigenfunctions for the conduction (valence) energy bands which can be expanded by Bloch orbitals $\Phi_j(\mathbf{k}, \mathbf{r})$ at the A and B lattice sites of the 2D graphite unit cell

$$\Psi^i(\mathbf{k}) = \sum_{j=A,B} C_j^i(\mathbf{k})\Phi_j(\mathbf{k}, \mathbf{r}), \quad i = \mathrm{c}, \mathrm{v}\ . \tag{19}$$

Furthermore, the Bloch orbital can be expanded by a tight binding wavefunction and thus the dipole vector can be a sum of atomic dipole vectors [29]. The unique feature of an optical transition in graphite and in SWNTs comes not from the atomic wavefunction but from the Bloch coefficient $C_j^i(\mathbf{k})$, and we do not go into the details of the calculation for $C_j^i(\mathbf{k})$ here.

4.3.1. Node for optical transitions in 2D graphite and SWNTs

Optical absorption or emission in 2D graphite occurs at an equi-energy line near the K point in the 2D Brillouin zone (see Fig. 7), since the valence and conduction energy bands touch each other at the K point. An important fact for the two coefficients of the Bloch wavefunctions for the A or B sites, $C_j^i(\mathbf{k})$ ($j = \mathrm{A}, \mathrm{B}$), is that the $C_j^i(\mathbf{k})$ coefficients are either constant or linearly proportional to the magnitude of $\mathbf{k}$, as measured from the K point. As a result, the dipole vector is a linear function of k_x (or k_y) in the case of 2D graphite $(-k_y, k_x, 0)$. For linear polarization $\mathbf{P} = (p_x, p_y, p_z)$, the matrix element of Eq. (18) has a k dependence of $k_x p_y - k_y p_x$. This fact tells us that the optical absorption (or emission) matrix element $M^{\mathrm{d}}(\mathbf{k})$ has a node at the crossing point of an equi-energy circle around the K point with the line $k_x p_y - k_y p_x = 0$. Thus the node position is rotated by the polarization direction $\mathbf{P}$ [29].

It is not easy to observe the existence of such a node by optical measurements in 2D graphite, since we normally observe the optical absorption for all $\mathbf{k}$ states on the equi-energy contour. However, if we have a special graphite sample with a lower dimension than two, the k vector becomes discrete and thus we can find the node by rotating $\mathbf{P}$. Recently Cançado et al. observed this node by using a thin graphite

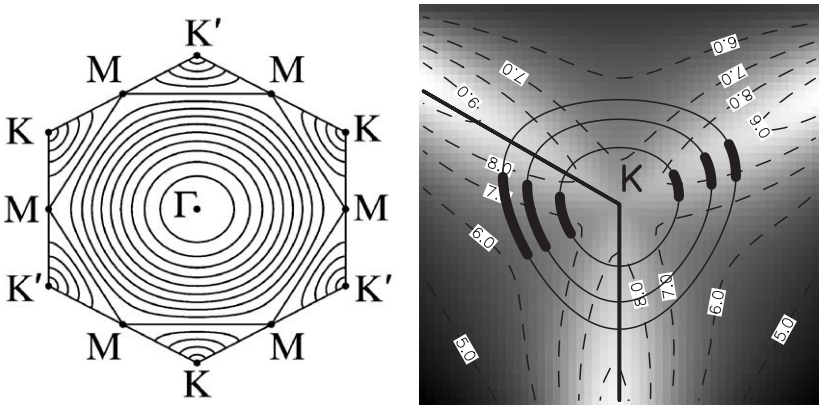

(a) (b)

Fig. 7. (a) Equi-energy contour plot for π electrons in the 2D graphite BZ. (b) Magnitude of the electron–photon matrix element as a function of the vHS k points of SWNTs. Numbers on the various contours label the values of the electron–photon matrix elements in arbitrary units.

(nano-graphite) ribbon [31]. Since the graphite ribbon has a very small width in one direction, the wave vector becomes discrete in this direction. Thus by rotating the polarization relative to the ribbon direction, oscillations in the absorption intensity could be observed experimentally [31].

In the case of isolated SWNTs, we expect a similar observation to that in nano-graphite. However, because of the curvature of the cylindrical SWNT surface, the atomic dipole vectors do not have the same direction as they do in planar 2D graphite. Thus we do not generally expect to observe the node that is found in the 2D graphite BZ.

Nevertheless, the analytic expression for the matrix element has a node if we plot the matrix element as a function of **k** in the 2D Brillouin zone [30], but the node in this case comes from a completely different origin, which is not discussed in this review in detail. An important result is that the matrix element for perpendicular polarization has a node at the vHS k points at which we expect a strong absorption for parallel polarization. Until now, we have understood that the optical absorption is suppressed for perpendicular polarization because of a complete screening by charge induced by the electric field on the cylindrical SWNT surface (depolarization effect) [32,33]. If the matrix element is zero at the vHS points, the main contribution of the suppression of the optical absorption may be understood by the vanishing $M^{\mathrm{d}}(\mathbf{k})$ matrix element [30].

4.3.2. Diameter and chirality dependence of optical processes

Recent photoluminescence (PL) measurement of semiconducting carbon nanotubes show a diameter dependence (the smaller the diameter, the stronger the intensity) and a chirality dependence (the closer to the armchair direction, the stronger the intensity) of the PL intensity [34]. This dependence of the PL intensity is dependent on the electron–photon matrix element calculation where the value of the matrix element at the vHS is relevant for the peak PL intensity.

In Fig. 7(b), we plot the value of the matrix element as a function of the vHS points for many SWNTs around the K point in the BZ, for optical polarization parallel to the nanotube axis, while in Fig. 7(a), we show equi-energy contours of π electrons in 2D graphite. A vHS point corresponds to the touching point of the cutting line for each (n, m) with an equi-energy contour line (see Section 2.2). When we consider the chiral angle between $\theta = 0°$ (zigzag) and 30° (armchair) on the three equi-energy contours shown in Fig. 7(b), the bold solid curves correspond to vHS positions. The inner circle corresponds to the smallest laser energy and thus to a resonance with the largest diameter SWNTs. The bold curves in the left (inside the hexagonal BZ) and those on the right (outside of the BZ) correspond to vHSs for different types of semiconductor nanotubes depending on (n, m). These types are denoted by MOD1 [mod$(2n + m,3) = 1$] or MOD2 [mod$(2n + m,3) = 2$] semiconducting SWNTs, respectively [35].

As can be seen in Fig. 7(b), the electron–photon matrix element has a larger value in the three directions from K to the M points than from K to the Γ points. The matrix element values increase with increasing distance from the K point in k space, corresponding to the experimental fact that smaller diameter SWNTs give stronger optical absorption and photoluminescence (PL). PL spectra are usually observed at the energy of the lowest vHS for isolated semiconducting SWNTs, E_{11}^{S}. It is known that the E_{11}^{S} energy position in k space is either along the $K - M$ side or the $K - \Gamma$ side, respectively, depending on whether the SWNT belongs to class MOD1 [mod$(2n + m,3) = 1$] or to class MOD2 [mod$(2n + m,3) = 2$] semiconducting SWNTs (see Fig. 4) [35]. Thus for a similar diameter SWNT, the PL intensity is stronger for MOD1 than MOD2 SWNTs, which is consistent with the experimental results [36]. However, the chirality dependence of the intensity predicted from the matrix element calculation is not as large as the experimental observations. Thus a strong chirality dependence may come from the supposition that the

abundance of SWNTs is large for semiconducting SWNTs near $\theta = 30°$. In fact, the abundance of a SWNT seems to be determined by the stability of its cap, which might be important as an initial condition of the SWNT synthesis process.

4.4. Electron–phonon matrix elements

Next we consider the electron–phonon matrix element for an electron in the conduction band. Initially, the electron is in a $\mathbf{k}$ state on the energy-contour around the K (or K') point for photo-excited states. The scattered $\mathbf{k} - \mathbf{q}$ states are energy-momentum conserving electronic states obtained by emitting a phonon with wave vector $\mathbf{q}$ and energy $\hbar\omega(\mathbf{q})$. The electron–phonon matrix element is given by

$$M_j^{\mathrm{ep}}(\mathbf{k}, \mathbf{k} - \mathbf{q}) = A_j \mathbf{u}_q^j \cdot \langle \Psi^{\mathrm{c}}(\mathbf{k} + \mathbf{q}) | \nabla V(r) | \Psi^{\mathrm{c}}(\mathbf{k}) \rangle \ , \tag{20}$$

in which $\langle \Psi^{\mathrm{c}}(\mathbf{k}+\mathbf{q}) | \nabla V(r) | \Psi^{\mathrm{c}}(\mathbf{k}) \rangle$ is the deformation potential (gradient of the crystal potential) vector, and A_j and $\mathbf{u}_{\mathbf{q}}^j$ are the amplitude and eigenvector of the phonon. For a given initial state in 2D graphite, there are six different phonon modes and two possible scattering paths, known as intra-valley and inter-valley scattering [22]. The final states are on circles around the K point whose size is slightly decreased relative to the initial energy contour by decreasing the energy of the contour by the phonon energy. In the case of a SWNT, $6N$ phonon states are involved, since the wave vector in the circumferential direction becomes discrete [1]. Each phonon mode is labeled by an irreducible representation of the C_N point group. Only A symmetry phonon modes contribute to the scattering within the 1D electronic energy band. The other E symmetry phonon modes contribute to interband transitions (see Section 4.3).

4.4.1. Electron–phonon scattering for first-order processes

In Fig. 8(a) we plot the calculated electron–phonon matrix element for graphite and for the case of a zone center phonon with wave vector $\mathbf{q} = 0$ in which the initial and final states can be approximated to be the same. Strictly speaking, it is not possible to plot this case while conserving energy and wave vector. However, since the excited electron energy relative to the Fermi energy (2 eV in this case) is much larger than the phonon energy (0.2 eV at most), we can use the $q = 0$ case for understanding the physics behind the electron–phonon matrix element for the first-order Raman intensity.

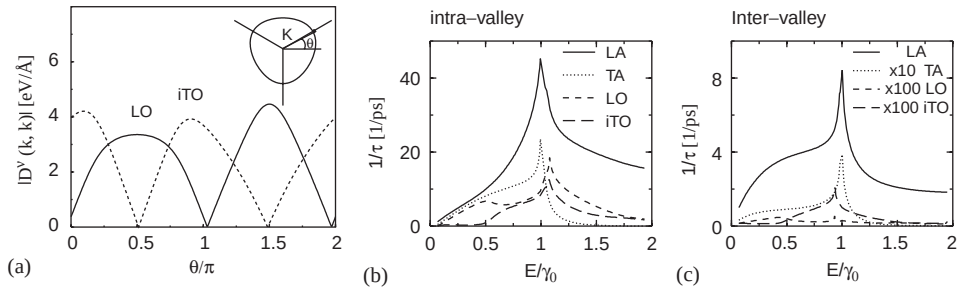

Fig. 8. (a) Calculated electron–phonon coupling constant for graphite for $q = 0$ around the K point, where 0 degrees corresponds to the k_x-axis. (b) Calculated intra-valley and (c) inter-valley contributions to the inverse of the electron relaxation time for four in-plane phonon modes $\gamma_0 = 2.89$ eV [30].

Because of the mirror symmetry of the graphite plane, the deformation potential vector lies within the graphite plane and thus the electron–phonon interaction for out-of-plane modes becomes zero. For $\mathbf{q} = 0$ phonons, the two in-plane acoustic phonon modes do not contribute to the electron–phonon coupling constant. Thus only the longitudinal optic (LO) and the in-plane tangential optical (iTO) phonon mode contribute to those electron–phonon modes for ($\mathbf{q} = 0$), that determine the *G*-band Raman intensity.

When the initial state rotates around the *K* points, the LO and iTO electron–phonon matrix elements oscillate alternatively, as shown in Fig. 8(a). Thus, the relevant phonon for the *G*-band signal depends on the **k** position. In the case of 2D graphite, however, we cannot distinguish between the contributions from the LO and iTO phonons to the Raman spectra. In the case of SWNTs, however, the LO and iTO phonon modes give rise to the G^+ and G^- spectra whose relative intensity I_{G^-}/I_{G^+} depends on the (n, m) chirality of the SWNT, since the vHS points shift with changing (n, m) as is seen in Fig. 4 [37]. The calculation of the electron–phonon matrix element shown in Fig. 8 is consistent with previous calculations of the chirality dependence of the *G*-band intensity [37].

4.4.2. Inter-valley electron–phonon scattering

When we consider inter-valley electron–phonon scattering processes, the G' band feature is very useful for explaining these processes. Since the G' band spectra arise from a two-phonon, inter-valley, second-order Raman scattering process, the G' spectra are free from defect effects, and the corresponding experimental signal is of comparable intensity to that of the *G* band.

We have calculated the Raman spectra for the G'-band of graphite by considering both electron–photon and electron–phonon coupling for two phonon-emitting processes [38]. In Fig. 9, we compare the experimental G' Raman spectra of a HOPG sample for 1.92, 2.18, 2.41, 2.54, and 2.71 eV

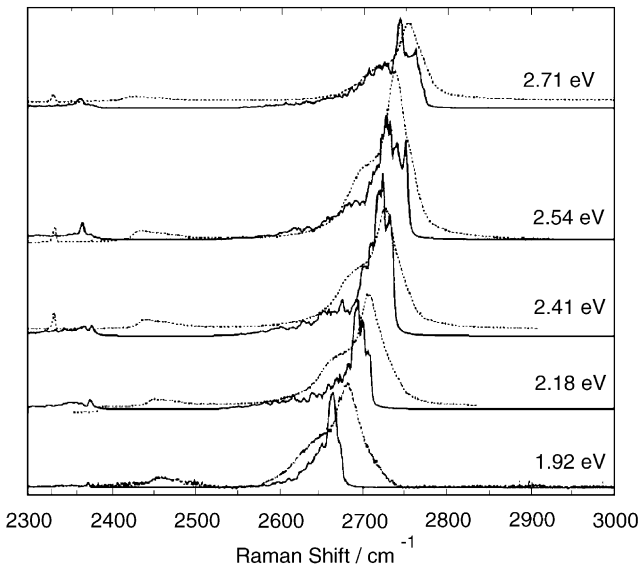

Fig. 9. The calculated (dotted) and experimental (solid) G' spectra in HOPG (highly oriented pyrolytic graphite) for several laser excitation energies E_L. The main peak appears at approximately 2700 cm^{-1} which is dispersive, while a weaker non-dispersive phonon mode appears around 2450 cm^{-1} [38].

excitation laser energy with the calculated results for the same laser energies [38]. The maximum intensity in the calculation is normalized to the experimental peak height. Both the calculated and experimental results show a peak shifting on the dispersive double resonance peak around 2700 cm^{-1} and little change for the non-dispersive peak around 2450 cm^{-1}. At 2.54 eV, the calculated peak feature and position agree well with the experimental results. The calculation indicates that this lower phonon frequency mode occurs around 2350 cm^{-1} and is due to the non-dispersive $q = 0$ Raman peak. It should be mentioned that the phonon dispersion relations that we used in this calculation are not perfectly satisfactorily in reproducing all features of the double resonance spectra. Moreover, the origin of the lower frequency feature can be a non-dispersive LO mode, a dispersive LA mode, or a combination of both (the LO and LA, that are degenerate at the K point). The only phonon branch which has such a dispersion in the observed frequency range is the LA branch. In fact, the electron–phonon matrix element for LA phonon modes has a maximum for $q = 2k$ and is zero for $q = 0$ in the case of planar graphite. However, in the case of SWNTs and DWNTs, the matrix elements are not exactly zero for small q values.

4.4.3. Non-radiative relaxation of electrons

Non-radiative relaxation of an electron is a scattering process of an electron by emitting a phonon. Since this process is much faster (in ps) than photon-emission process (in ns), no photo-luminescence occurs if there is a relaxation path for non-radiative relaxation. For example, there is no photoluminescence in metallic SWNTs. It is important for us to consider this relaxation when we compare the Raman spectra with photo-luminescence spectra.

We can use the same electron–phonon matrix element in the Raman intensity calculation for non-radiative relaxation. In graphite and SWNTs, the relaxation rate of an electron for phonon emission is on the order of 0.1 ps, which is much faster than an optical transition (0.1 ns), but much slower than electron–electron scattering (plasmon emission) (1 fs) for taking an electron in a higher energy electron state back to a state near the Fermi level. Hertel and coworkers reported fast optics measurements for photo-excited electrons, showing that the excited electron population at first decays very fast by electron–electron interaction and then decays more slowly through electron–phonon interaction by phonon emission [39].

Using the Fermi Golden Rule, we can calculate the lifetime for intra- and inter-valley electron–phonon scattering from a given k state using four in-plane phonon modes [30]. In Figs. 8(b) and (c), we plot the inverse of the lifetime for four in-plane phonon modes as a function of electron energy. The fastest recombination is for LA phonon modes both for intra-valley scattering [Fig. 8(b)] and for inter-valley scattering [Fig. 8(c)]. The electron–phonon coupling constant for the LA phonon mode increases quickly with increasing q values. The relaxation rate is singular around $E = 3$ eV, because of the singularity in the electronic density of states. The relaxation rate of an electron decreases with decreasing energy to the Fermi energy. It is a unique fact that in graphite the density of states near the Fermi energy (E_F) is proportional to E relative to E_F. When the electron energy decreases to the Fermi energy, the number of possible scattered states decreases to zero. Thus the lifetime increases with decreasing energy and finally at some electron energy the lifetime for electron–phonon processes becomes longer than the lifetime for photoluminescence, and below this energy, which corresponds to far infrared radiation, PL occurs [30]. This is the reason why carbon materials emit far IR light when they burn. In the case of metallic SWNTs, however, the electronic density of states is constant around the Fermi energy, and these arguments about the emission of IR radiation do not apply.

5. Raman spectroscopy experiments for carbon nanotubes

In this section we present an overview of Raman spectroscopy experiments for carbon nanotubes. In general, contributions to the Raman signal from resonance Raman processes are very much larger than contributions from non-resonance processes. This is especially the case for SWNTs, where the resonance condition for a vHS energy position of a given (n, m) nanotube is satisfied only within a small region of laser energy excitation, such as $\Delta E_L \sim 10$ meV. Thus, when we observe an isolated nanotube (n, m) SWNT on a substrate, the probability for a given E_L energy to satisfy the resonant condition is very small (less than 1%). For a bundle sample whose diameter distribution is known, an appropriate E_L energy can be selected so that both the RBM and *G*-band will be observed at the same time as long as the E_L is within the energy window of E_{ii} in the Kataura plot (Fig. 4).

For a straight isolated SWNT or for aligned SWNT bundles, we can change the direction of the optical electric field relative to the nanotube axis so that polarized Raman spectra can be taken. Both linear polarization and circular polarization are of particular interest. In both geometries, changes in the optical dipole selection rules can be observed and studied (see Section 4.2).

For resonance Raman spectroscopy, a tunable laser system, which can vary E_L quasi-continuously [40] is very powerful for probing a resonant (n, m) within a mixed SWNT sample. In second-order Raman processes, we have the possibility to change the phonon $\mathbf{q}$ corresponding to a particular (n, m) SWNT by changing E_L. By changing the diameter and chirality of SWNTs in general, we can observe many different resonance Raman spectra, which can be systematically analyzed. On the other hand, by measuring the dependence of many of the Raman features on the nanotube diameter and chirality, we can evaluate and characterize a given nanotube sample in some detail by resonance Raman spectroscopy.

In the following sections, we briefly review the many Raman features observed in the Raman spectra of carbon nanotubes, addressing the carbon nanotube physics that can be learned from their Raman spectra. In Section 5.1 a very brief coverage of the synthesis of carbon nanotubes is given and how Raman spectroscopy can be used for characterization purposes, including a connection to the synthesis and purification processes (Section 5.1). A brief review is included on how the experiments are done (Section 5.2) and how the Raman spectra are analyzed (Section 5.3). Section 6 focuses on the two strong features, the radial breathing mode and the *G*-band which are both first-order Raman features and not dispersive for a given (n, m) SWNT (see Section 3.1). In contrast, Section 7 reviews what we learn about carbon nanotubes from the rich spectrum of weaker double resonance features that tend to be dispersive, i.e., the Raman feature shifts position with a change in the frequency of the exciting laser (see Section 3.3).

5.1. Sample preparation

Carbon nanotube bundled samples can be synthesized by different methods, including chemical vapor deposition (CVD), laser vaporization and electric arc methods [2]. Isolated single-wall carbon nanotubes (SWNTs) are grown on a Si/SiO_2 substrate containing catalytic iron nano-particles [41], using a CVD method (diameters ranging from about 1 to 3 nm, according to atomic force microscopy (AFM) characterization) [3]. The density of SWNTs per μm^2 can be controlled during the growth process, basically by controlling the time of growth. Sonication of SWNT bundle samples in solution can also form isolated SWNTs. Wrapping nanotubes with, for example, sodium dodecyl sulfate (SDS) surfactant guarantees that tubes previously separated by sonication will not rejoin [34].

Raman spectroscopy is commonly used for characterizing SWNT bundles because it is one of the most sensitive characterization tools for these nanostructures [13,17]. The Raman experiment is simple, can be done at room temperature and under ambient pressure, is quick, non-destructive and non-invasive, and the instrumentation is generally available to a wide user community [13]. The technique has the sensitivity to probe differences in the properties of nanotubes prepared by different methods and under different conditions. For example, for "dirty" samples (full of amorphous carbon, catalyst or any other impurities), it is common that high laser powers ($10\,\mathrm{mW}\mu\mathrm{m}^{-2}$) can be used to burn impurities first, leaving cleaner SWNT samples behind [42]. This process can be checked by an improvement in the characteristic Raman signal of the sample when the incident laser power is slowly increased. Raman spectroscopy becomes even more powerful for isolated SWNTs, by providing detailed and accurate structural and electronic characterization [15].

5.2. *Micro-Raman spectroscopy*

Resonance Raman spectra from SWNTs can be acquired using standard commercial micro-Raman spectrometers and lasers. Typical measurements use a back-scattering configuration and 50×, 80×, and 100× objective lenses ($\sim 1\,\mu\mathrm{m}$ spot size for the 100× objective). Relatively high laser powers (up to $40 \times 10^9\,\mathrm{W\,m^{-2}}$) can be used to probe isolated SWNTs on substrates or in aqueous solution, because of their unusually high thermal conductivity values ($3000\,\mathrm{W\,mK^{-1}}$) [43], their excellent high temperature stability, and their good thermal contact to the environment. A triple monochromator is ideal for the Raman measurements while tuning the excitation laser line continuously, but the acquired intensity drops substantially when compared to the intensity obtainable from a single-monochromator spectrometer. We have measured the Raman spectra from SWNTs taken with many different laser lines using both discrete lines from Ar–Kr and He–Ne lasers and a continuous range of excitation energies from both a Ti:Sapphire and a Dye laser. Stable nanotube Raman signals can be observed for laser powers impinging on the substrate using up to 40 mW into a 100× objective. Laser powers of about 10 mW are typically used, although measurements have been carried out successfully with laser power levels down to 1 mW ($\sim 1 \times 10^9\,\mathrm{W\,m^{-2}}$) and longer time scans.

Fig. 10(a) gives a general view of the Raman spectra from a sample of single-wall carbon nanotube bundles. The two dominant Raman features are the radial breathing mode (RBM) at low frequencies and the tangential (*G* band) multi-feature at higher frequencies. Other weak features, such as the disorder-induced *D* band, the *M* band (an overtone mode) and the iTOLA band (a combination of optical and acoustic modes) are also shown, and when the background intensity is increased, a rich Raman spectrum is observed for the intermediate frequency phonon modes (IFM) which lie between the RBM and *G*-band features [40]. The laser power used to measure the Raman spectra for SWNT bundles without burning the sample should be much lower than for isolated SWNTs, and is usually not higher than 1 mW using a 100× objective lens, because of the poor inter-tube thermal conductivity in SWNT bundles. The spectra of isolated SWNTs dispersed in aqueous solution exhibit sharper Raman peaks, and such data can be acquired with higher input power.

In the process of measuring the Raman spectra from isolated SWNTs on a Si/SiO_2 substrate using a fixed laser energy E_L [see Fig. 10(b)], we focus the laser spot on the substrate surface and we scan the sample until we observe the Raman signal from an isolated SWNT. The Raman intensity from SWNTs is usually buried under the noise, except for a few (n, m) SWNTs for which the resonance with the given E_L occurs strongly for the electronic states confined within van Hove singularities (vHSs). The

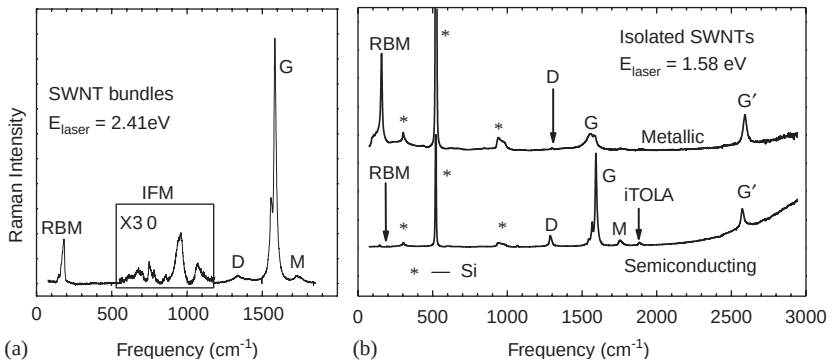

Fig. 10. (a) Raman spectra from HiPco SWNT bundles (see text) [44]. (b) Raman spectra from a metallic (top) and a semiconducting (bottom) SWNT at the single nanotube level. The spectra show the radial breathing modes (RBM), *D*-band, *G*-band and G' band features, in addition to weak double resonance features associated with the *M*-band and the iTOLA second-order modes [45]. The isolated carbon nanotubes are sitting on an oxidized silicon substrate which provides contributions to the Raman spectra denoted by "*", and these Si features are used for calibration purposes [3].

observation of the weak Si feature at 303 cm^{-1} is a useful guide for knowing whether the radial breathing Raman mode from an isolated SWNT can be measured. Fig. 10(b) shows an example of Raman signals from two resonant SWNTs at two different spots on the Si/SiO_2 surface. For various experiments of interest, we have used samples with a variety of nanotube densities, ranging from low-density samples ($\sim$ 0.4SWNT $\mu\mathrm{m}^{-2}$) to higher density samples ($\sim$ 10 SWNT $\mu\mathrm{m}^{-2}$). Samples with a high nanotube density (more than 1 SWNT $\mu\mathrm{m}^{-2}$) guarantee that the search for resonant nanotubes will not be so tedious, but a low-density sample (less than 1 SWNT $\mu\mathrm{m}^{-2}$) guarantees that one will not get a Raman signal from two or more SWNTs within the same light spot.

5.3. Raman spectra data analysis

In comparing the behavior of various features that are observed in the Raman scattering process for SWNTs the effect of the tube diameter on the mode frequencies must be considered. In this context, 2D graphite can be considered to be a tube with a diameter $d_t \to \infty$. The diameter dependence of the various mode frequencies is expressed by

$$\omega = \omega_0 + \beta/d_t^n \ , \tag{21}$$

in which ω_0, β, and n are the frequency of 2D graphite,[6] and the coefficient and exponent of the diameter dependence, respectively. Such information can be obtained by measurements at the single nanotube level as in Fig. 10(b). Table 3 displays results for the diameter dependence of the most common features observed in the Raman spectra of isolated SWNTs [see Fig. 10(b)]. For the double resonance *D*, G', *M* and iTOLA features in Fig. 10(b), the frequencies depend also on the excitation laser energy. Thus, when comparing results for different tube diameters, both the dependence of the phonon frequency on d_t and on E_L (if pertinent) must be considered. Only the parameters ω_0, n, and β are listed in Table 3.

[6] ω_0 is the value for $d_t \to \infty$. However, it does not always coincide with the value of 3D graphite because of the interlayer interaction of graphite. The value of ω_0 is obtained by the fitting of SWNT Raman data.

Table 3
Diameter dependence of Eq. (21) for the most common features observed in the Raman spectra of isolated SWNTs

Mode	Frequency ω_0 (cm^{-1})	Exponent n	Diameter coefficient β (cm^{-1} nm)
RBM	0	1	248[a]
D	1356	1	−16.5[b]
G^+	1591	0	0
G^-	1591	2[c]	(−45.7; −79.5)[d]
M^+	1754	1	−18.0[e]
M^-	1775	1	−16.7[e]
G'	2704	1	−35.4[b]

Here ω_0 denotes the mode frequency associated with 2D graphite, whose value depends on the laser excitation energy, if the mode is associated with a double resonance process. Frequencies are in units of cm^{-1}, and d_t is in units of nm. The coefficients for the D, M, and G' bands and for the RBM feature were obtained by using data measured at the single nanotube level with $E_{L_i} = 2.41$ eV.

[a]Ref. [3].

[b]This value was obtained using $E_L = 2.41$ eV. By using the spectra obtained with 1.58 eV, a $\beta = -18.9\,cm^{-1}$ nm value was obtained Ref. [46].

[c]The coefficient $n = 2$ was found by analyzing the G band with only two Lorentzian peaks [47]. A different value is found when using the six symmetry-allowed peaks to fit the G-band spectra [26] (see Section 6.2.2).

[d]The coefficient β for the G^- component is, respectively, −45.7 and $-79.5\,cm^{-1}\,nm^2$ for semiconducting and metallic SWNTs, and 1.58, 2.41, and 2.54 eV laser lines were used to obtain the G-band experimental results used in the fitting procedure [47].

[e]Ref. [45].

The Raman features are analyzed by a Lorentzian fit of the spectra, with the exception of the lower-frequency G-band feature for metallic SWNTs, denoted by G^-, which is observed to have a Breit–Wigner–Fano (BWF) lineshape (broad and asymmetric peak) (see Section 3.6), though the G^- feature for semiconducting SWNTs remains Lorentzian. Although it is known that the disorder-induced bands appear in the Raman spectra of graphite-like materials through a double resonance process [18,22] where inhomogeneous broadening occurs, we use the Lorentzian fit as an approximation to interpret their behavior.

6. Learning about carbon nanotubes from their first-order Raman features

6.1. The radial breathing mode

The radial breathing mode (RBM) can be used to study the nanotube diameter (d_t) through its frequency (ω_{RBM}), to probe the electronic structure through its intensity (I_{RBM}) and to perform an (n, m) assignment of a single isolated SWNT from analysis of both d_t and I_{RBM}, as discussed below.

6.1.1. The RBM frequency and nanotube diameter

The radial breathing mode (RBM) Raman features correspond to the coherent vibration of the C atoms in the radial direction, as if the tube were “breathing”. These features are unique to carbon nanotubes and occur with frequencies ω_{RBM} between 120 and 350 cm^{-1} for SWNTs for diameters in the range

$0.7\,\text{nm} < d_t < 2\,\text{nm}$. These RBM frequencies are therefore very useful for identifying whether a given carbon material contains SWNTs, through the presence of RBM modes, and for characterizing the nanotube diameter distribution in the sample through use of the relation $\omega_{\text{RBM}} = A/d_t + B$, where the A and B parameters are determined experimentally [3,48]. For typical SWNT bundles in the diameter range $d_t = 1.5 \pm 0.2\,\text{nm}$, $A = 234\,\text{cm}^{-1}\,\text{nm}$ and $B = 10\,\text{cm}^{-1}$ has been found [48] (where B is an upshift in ω_{RBM} assigned to tube-tube interactions). For isolated SWNTs on an oxidized Si substrate, $A = 248\,\text{cm}^{-1}\,\text{nm}$ and $B = 0$ has been found [3,49]. It is important to point out that, for the usual diameter range $1 < d_t < 2\,\text{nm}$, these two sets of parameters give similar d_t for a given ω_{RBM}, differing considerably only for $d_t < 1\,\text{nm}$ and $d_t > 2\,\text{nm}$. However, for $d_t < 1\,\text{nm}$, the simple $\omega_{\text{RBM}} = A/d_t + B$ relation is not expected to hold exactly, due to nanotube lattice distortions leading to a chirality dependence of ω_{RBM} [50]. For large diameter tubes ($d_t > 2\,\text{nm}$), the intensity of the RBM feature is weak and is hardly observable.

Therefore, from the ω_{RBM} measurement of an individual isolated SWNT, it is possible to obtain its d_t value. As discussed in Section 6.1.3, it is actually possible to obtain the full assignment (n, m) for an individual isolated SWNT. The natural linewidth (FWHM) for isolated SWNTs on a SiO_2 substrate is $\gamma = 3\,\text{cm}^{-1}$ [51], but much sharper linewidths (down to $\sim 0.25\,\text{cm}^{-1}$) have been observed for the inner tubes of double wall carbon nanotubes (DWNTs) [52].

The RBM spectra for SWNT bundles [Fig. 10(a)] contain an RBM contribution from different SWNTs in resonance with the excitation laser line. For a diameter characterization of the sample, analysis of the resonance condition should be performed, and as discussed in Section 2.2, it is useful to have a Kataura (E_{ii} vs. d_t) plot (Fig. 4) on hand when acquiring the RBM spectra from a SWNT sample [13]. It is clear that a single Raman measurement gives an idea of the tubes that are in resonance with that laser line, but does not give a complete characterization of the diameter distribution of the sample. However, by taking Raman spectra using many laser lines, a good characterization of the diameter distribution in the sample can be obtained [48]. Since semiconducting (S) and metallic (M) tubes of similar diameters do not occur at similar E_{ii} values, ω_{RBM} measurements using several laser energies E_{L} can be used to characterize the ratio of metallic to semiconducting SWNTs in a given sample [53].

6.1.2. The I_{RBM} and the electronic structure

The resonance Raman intensity depends on the density of electronic states (DOS) available for the optical transitions, and this property is very important for 1D systems, as discussed in Sections 2.2 and 3.2. By using a tunable laser, it is possible to study the joint density of states (JDOS) of *one* isolated SWNT, giving the E_{ii} value with a precision better than 5 meV as shown in Fig. 11(a). Here fiducial markers were used [Fig. 11(b)] to achieve good precision by always returning the light spot of the excitation laser to the same position on thesample, as the laser energy E_{L} is changed. To obtain the data points in Fig. 11, Raman spectra of the sample were measured in the excitation wavelength (energy) range from 720 nm (1.722 eV) to 785 nm (1.585 eV) in steps of 4 nm ($\sim$ 9 meV) [54]. The resonance profile could then be fit to obtain the relevant parameters describing the profile, including E_{ii} (see the Kataura plot, Fig. 4; $E_{ii} = E_{aj}$ in Section 4.1) and the width of the resonance window energy γ, which is defined as the full-width half-maximum (FWHM) intensity range in energy over which a given (n, m) nanotube is in resonance. Stokes (phonon emission) and anti-Stokes (phonon absorption) spectra were taken to increase the accuracy in the determination of E_{ii} at each laser energy [55]. Fig. 11 shows that the resonance windows for the Stokes and anti-Stokes processes have a small width ($\gamma =$ 8 meV) and are asymmetric. This asymmetric behavior is caused by the asymmetry in the joint density of

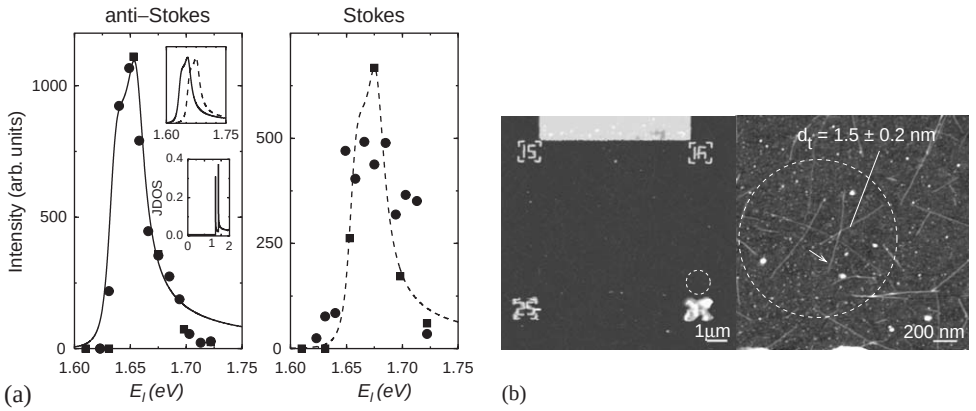

Fig. 11. (a) Raman intensity vs. laser excitation energy for the $\omega_{\mathrm{RBM}} = 173.6\,\mathrm{cm}^{-1}$ peak in the Stokes and anti-Stokes Raman processes for one SWNT on a SiO_2 substrate. To account for the T dependence of the phonon absorption process, so that the experimental Stokes and anti-Stokes intensities can be directly compared, the anti-Stokes intensities were multiplied by $[n(\omega)+1]/n(\omega)$, where $n(\omega) = 1/[\exp(\hbar\omega/k_{\mathrm{B}}T) - 1]$ is the Bose–Einstein thermal factor (see Section 3.5), ω is the phonon frequency, k_{B} is the Boltzmann constant, and T is the sample temperature. The line curves indicate the resonant Raman windows from which $E_{ii} = 1.655\,\mathrm{eV}$ and a width for the window $\gamma = 8\,\mathrm{meV}$ were determined (see Section 4.1). The upper inset compares the theoretically predicted Stokes and anti-Stokes resonance windows. The lower inset plots the JDOS for one isolated $(18, 0)$ SWNT with a width $\gamma_{\mathrm{J}} = 0.5\,\mathrm{meV}$ taken for the van Hove singularity [54]. (b) The left AFM image shows the markers used to localize the spot position (dashed circle) on the SiO_2 substrate during the Raman experiment and used for further AFM characterization of the SWNTs present in the light spot (right image).

states (JDOS)

$$g(E) = \frac{C}{\sqrt{(E + E_{ii} + i\gamma_{\mathrm{J}})(E - E_{ii} - i\gamma_{\mathrm{J}})}}\ , \tag{22}$$

where each van Hove singularity has an energy width γ_{J} [54]. The upper inset in Fig. 11 shows a comparison between the theoretically obtained Stokes and anti-Stokes resonant windows, revealing a shift in these resonant windows due to the resonance condition for the scattered photon, $E_{\mathrm{s}} = E_{ii} \pm E_{\mathrm{ph}}$ for the anti-Stokes (+) and the Stokes (–) processes (see Sections 3.2 and 3.5). The lower inset to Fig. 11 plots the highly singular JDOS vs. laser excitation energy E_{L} for the isolated $(18, 0)$ SWNT, as measured in this experiment.

Resonance Raman experiments with a tunable system can give E_{ii} with high accuracy ($\sim \pm 3\,\mathrm{meV}$). A much simpler experiment, however, that just involves measuring Stokes vs. anti-Stokes Raman signals with a single laser line at the isolated SWNT level, allows the determination of E_{ii} within $\pm 10\,\mathrm{meV}$ precision for SWNTs sitting on a Si/SiO_2 substrate [13,55,56]. The precision for this assignment using Stokes vs. anti-Stokes Raman measurements depends on a detailed determination of the shape of the resonance window. The resonance window profile is however sensitive to the sample substrate, sample preparation methods, whether the SWNT is wrapped by a surfactant or other species, or whether or not the SWNT is freely suspended, as discussed in Section 6.1.4.

The E_{11}^{S} energy value for semiconducting SWNTs is usually too small to be observed with standard Raman spectroscopy setups. The observation of E_{11}^{S} is however in a convenient range for photoluminescence experiments [34]. The spectral interdependence of the absorption and emission energies generate intense

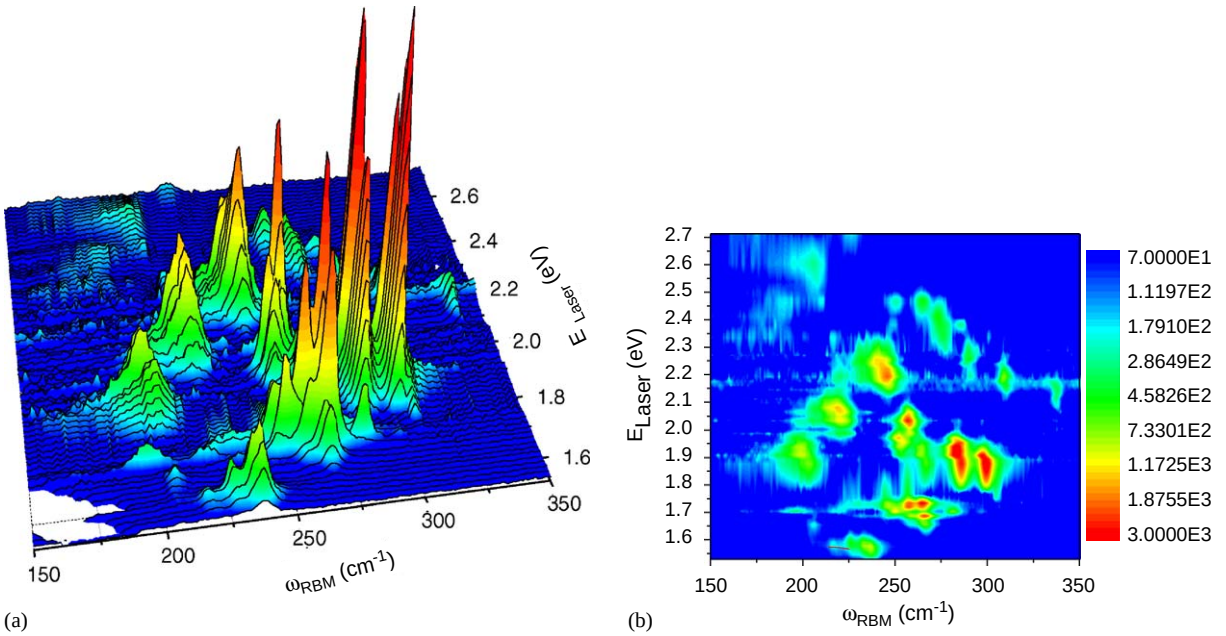

Fig. 12. (a) RBM Resonance Raman measurements of HiPco carbon nanotubes wrapped in sodium dodecyl sulfate (SDS) and dispersed in an aqueous solution [34], measured with 76 different laser lines E_{L} [44]. The non-resonance Raman spectrum from a CCl_4 solution, physically separated from the nanotube sample, is acquired after each RBM measurement, and the CCl_4 features are used to calibrate the spectral intensities and to check the frequency calibration with high resolution (better than $0.5\,\mathrm{cm}^{-1}$) [44]; (b) Top view of (a). Colors (see scale on the right) indicate the Raman intensity.

peaks on a 2D plot [57]. The results indicate strong optical absorption at a given E_{ii} and strong emission at E_{11}, each peak related to one specific (n, m) SWNT. Photo-luminescence (PL) as a characterization tool is limited to systems where non-radiative electron–hole recombination does not readily occur, so that light emission from metallic SWNTs or from SWNTs in bundles cannot be observed.

6.1.3. The RBM and the (n, m) assignment

By considering the d_t values obtained from measurements of ω_{RBM}, and $E_{ii} \sim E_{\mathrm{L}}$ from the resonance condition, the RBM feature can be used for making (n, m) assignments for individual isolated SWNTs [3], by utilizing a Kataura plot, such as in Fig. 4. In Fig. 10(b), the spectra are taken with a laser excitation of $E_{\mathrm{L}} = 1.58\,\mathrm{eV}$ (785 nm), and the observed RBM for the upper spectrum is assigned to a metallic (13, 10) SWNT with $d_t = 1.59\,\mathrm{nm}$, where E_{L} is in resonance with E_{11}^{M}. In contrast, the lower spectrum in Fig. 10(b) comes from a semiconducting (23, 1) SWNT, where E_{L} is in resonance with E_{33}^{S}. For a better understanding of the (n, m) assignment procedure, we discuss the formation of a E_{ii} vs. ω_{RBM} 2D plot (Fig. 12), that can easily be related to the Kataura plot (Fig. 4).

Fig. 12 presents Stokes resonance Raman measurements of carbon nanotubes grown by the HiPco process [58], wrapped with a surfactant sodium dodecyl sulfate (SDS) and dispersed in an aqueous solution [34], in the frequency region of the RBM features. For this experiment, a triple-monochromator spectrometer and a tunable laser system were used to obtain an almost continuous change of the excitation laser energies (E_{L}) in the range between 1.52 up to 2.71 eV. Using 76 values of E_{L} in this range, detailed

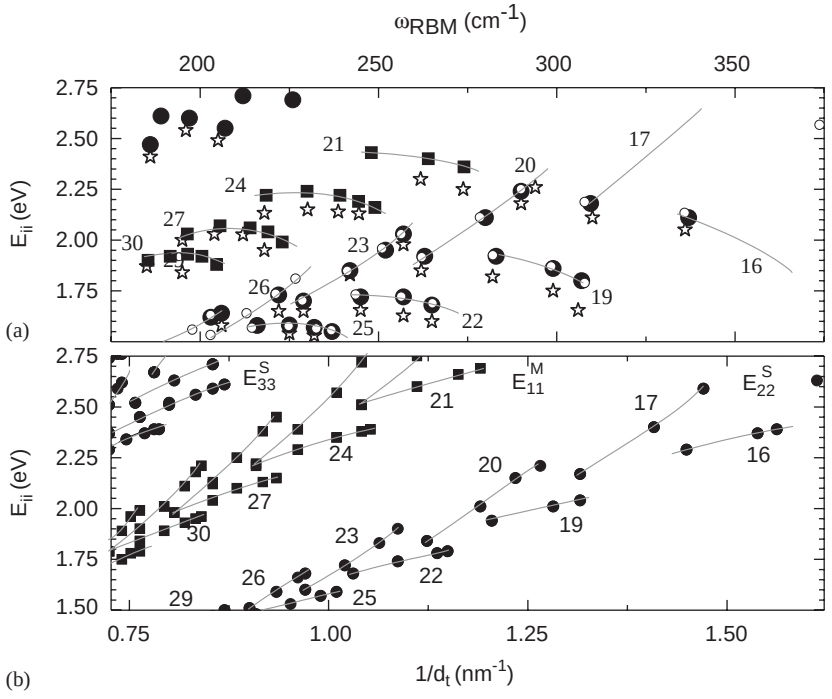

Fig. 13. (a) The points denote 47 electronic transition energies E_{ii} vs. ω_{RBM} for 41 different (n, m) carbon nanotubes measured by resonance Raman spectroscopy. Black circles and black squares, respectively, denote semiconducting and metallic HiPco SWNTs wrapped with SDS in aqueous solution. Open stars are for HiPco SWNTs in bundles. Open small circles are the photoluminescence results for SWNTs wrapped in SDS [59] (see text). Solid lines delineate nanotubes belonging to families of constant $(2n + m)$. (b) Plot similar to (a) based on the tight binding model using the tight binding parameters $\gamma_0 = 2.9\,\mathrm{eV}$, $s = 0$ and $a_{\mathrm{C–C}} = 0.142\,\mathrm{nm}$ [1].

information about the evolution of the RBM Raman spectra as a function of E_{L} is obtained. Several RBM peaks appear in Fig. 12, each peak corresponding to a SWNT in resonance with E_{L}, thereby delineating for each nanotube the resonance window, as shown in Fig. 11(a).

Fig. 13(a) plots the experimental results obtained for E_{ii} vs. ω_{RBM} for each (n, m) resonant nanotube in Fig. 12. Black circles and squares represent, respectively, semiconducting and metallic HiPco nanotubes wrapped in SDS. The different E_{ii} electronic transitions for semiconducting (E^{S}_{22} and E^{S}_{33}) and metallic (E^{M}_{11}) tubes [see Fig. 13(a)] are clearly seen. For nanotubes with diameters smaller than 1.2 nm, geometrical patterns can be seen in Fig. 13(a) for carbon nanotube families with $(2n+m)$= constant (solid lines) for the E^{S}_{22} and E^{M}_{11} transitions. It is possible to distinguish in Fig. 13(a) the three classes of nanotubes: metallic MOD0 [$(2n+m)$; mod $3=0$], semiconducting MOD1 [$(2n+m)$; mod $3=1$] and semiconducting MOD2 [$(2n+m)$; mod $3=2$] SWNT (see solid lines) [11]. These three classes of nanotubes exhibit different E_{ii} behaviors, as discussed in Section 2.2 (see Fig. 4). The (E_{ii}, ω_{RBM}) results [Fig. 13(a)] can be compared with one-electron, first-neighbor tight binding (TB) predictions [Fig. 13(b)] [1]. Although the energies do not match due to the simplicity of the tight binding calculations, the experimentally observed geometrical patterns for the families in Fig. 13(a) can be compared with the predicted geometrical patterns in Fig. 13(b), and the comparison leads to a clear (n, m) assignment.

The electronic transition energies E_{11}^{M} for metallic SWNTs are also determined by resonance Raman spectroscopy (RRS) [black squares in Fig. 13(a)]. The formation of families of constant $(2n+m)$ is also observed for metallic SWNTs with $d_t \leqslant 1.2$ nm. Surprisingly, the expected splitting in the E_{11}^{M} van Hove singularities caused by the trigonal warping effect [2,35] [see Fig. 13(b)] is not observed optically for the RBM feature, but only the lower energy component of E_{11}^{M} for each (n,m) SWNT [Fig. 13(a)] is observed experimentally in the Raman spectra.

From the (n,m) assignment for both metallic and semiconducting SWNTs, the relation $\omega_{RBM} = 228/d_t + 16\,\mathrm{cm}^{-1}$ is obtained between the RBM frequency and the nanotube diameter for these small diameter SWNTs wrapped with SDS [44]. The deviation of the experimental points from this relation is on the order of 1% of ω_{RBM}, and this deviation is related to a weak dependence of ω_{RBM} on chirality [60], that is observed in small diameter SWNTs due to curvature effects, as predicted by Kürti et al. [50].

6.1.4. RRS vs. PL and environmental effects on RBM spectra

Raman spectroscopy, optical absorption and photoluminescence have all been used to determine the E_{ii} energy values, leading to the development of theoretical models to describe the nanotube electronic structure for excited states. However, the E_{ii} values of an (n,m) SWNT are found to shift by an unexpectedly large amount (up to ~100 meV) by the effects of the substrate, of bundling, and of other environmental factors surrounding the SWNTs such as solvents and wrappings. Furthermore, early determinations of E_{ii} values from photoluminescence measurements on SDS wrapped SWNTs in solution were not in good agreement with Raman measurements on isolated tubes on a Si/SiO_2 substrate. To minimize environmental effects associated with different substrates and wrapping agents, E_{ii} values were experimentally determined from both Raman spectra and photoluminescence (PL) spectra taken for SWNTs originating from the same type of HiPco SWNT starting material, and wrapped in SDS, in the same way. Thus the E_{ii} values obtained by resonance Raman spectroscopy and photoluminescence on the same SWNTs in the same environments could be compared in detail. The black dots and squared in Fig. 13(a) are results measured by the Raman effect. The open circle points in Fig. 13(a) are for E_{22}^{S} transitions in SDS wrapped nanotubes in aqueous solution obtained by photoluminescence (PL) experiments [57,59] making use of the ω_{RBM} and d_t values obtained from $\omega_{RBM} = 228/d_t + 16\,\mathrm{cm}^{-1}$ [44]. Good agreement overall was obtained between the E_{ii} values obtained from resonance Raman spectroscopy (RRS) and photoluminescence (PL) data (taken on similar samples and under similar environmental conditions) [44]. The largest deviation between E_{ii} obtained by Raman and PL is 35 meV, and this is for the (6,4) SWNT, which has a small diameter. This experiment confirmed that the same excited states participated in the PL and resonance Raman processes.

In a second set of experiments, the resonance Raman spectra for an as-grown HiPco SWNT bundle sample without SDS wrapping were also measured. For these samples both Stokes and anti-Stokes Raman spectra were also taken and analyzed to yield E_{ii} values [44]. No significant change in ω_{RBM} was observed, as shown by the star symbols in Fig. 13(a), between the bundled HiPco sample and the SDS wrapped HiPco SWNTs. However, when the corresponding E_{ii} comparison was made between the RRS spectra for HiPco SWNTs in bundles and the corresponding spectra for SDS wrapped HiPco SWNTs in solution, a considerable red-shift was observed (20–120 meV) for the SWNTs in bundles. Furthermore, the E_{ii} values for the SWNTs in bundles, were actually found to be strongly dependent on laser power, i.e., on the local temperature [44], showing a strong temperature dependence of the resonance window for SWNT bundles. By increasing the laser power, the E_{22}^{S} energies were increasingly red-shifted for MOD1 nanotubes and blue-shifted for MOD2 nanotubes, relative to the average 70 meV red-shift that was observed overall.

These results showed that the trigonal distortion of the electronic structure, or equivalently the spread of the families for the E_{22} transition at constant diameter, increases with temperature [44].

With respect to the spectral linewidths, it is observed that the Raman resonance windows for SDS wrapped[7] ($\sim$ 60 meV) and bundled ($\sim$ 98 meV) SWNTs [44] are much broader than those for bare-isolated nanotubes ($\sim$ 8 meV) [54], showing the influence of the inhomogeneous nanotube environment on the electronic structure of SWNTs. Optical absorption and emission measurements on carbon nanotube samples show peaks corresponding to E_{ii} values for individual (n, m) SWNTs, with linewidths of $\sim$ 25 meV, comparable to the room temperature thermal energy [34,57,59,61], while measurements on suspended SWNTs show much sharper linewidths [62]. The accuracy of the E_{ii} determination is, therefore, dependent on sample environment and experimental technique.

From these results, we conclude that environmental effects cannot be neglected in comparing resonance Raman spectroscopy (RRS) and photoluminescence (PL) experiments with each other and independently. In order to compare all experimental results consistently, environmental effects should be formulated by a simple function by collecting various experimental data. Because of the different diameter distributions, different environmental conditions, and different experimental conditions under which the Raman spectra in the literature were taken, further effort is needed to interrelate the information provided by the various spectra now present in the literature. A table showing experimental values for ω_{RBM}, E_{11}^{M}, E_{22}^{S} and the (n, m) assignments, obtained for both semiconducting and metallic nanotubes wrapped in SDS is presented elsewhere [44,63].

6.2. The G-band

The *G*-band in graphite involves an optical phonon mode between the two dissimilar carbon atoms A and B in the unit cell. The corresponding mode in SWNTs bears the same name. In contrast to the graphite Raman *G* band, which exhibits one single Lorentzian peak at 1582 cm^{-1} related to the tangential mode vibrations of the C atoms, the SWNT *G*-band is composed of several peaks due to the phonon wave vector confinement along the SWNT circumferential direction and due to symmetry-breaking effects associated with SWNT curvature [see Figs. 14(a) and 15]. The *G*-band frequency can be used for (1) diameter characterization, (2) to distinguish between metallic and semiconducting SWNTs, through strong differences in their Raman lineshapes [13,56]; (3) to probe the charge transfer arising from doping a SWNT; and (4) to study the selection rules in the various Raman scattering processes and scattering geometries. These topics are reviewed in this subsection.

6.2.1. The G-band lineshape and diameter dependence

Fig. 14(b) indicates that the *G*-band feature for SWNTs consists of two main components, one peaked at 1590 cm^{-1} (G^+) and the other peaked at about 1570 cm^{-1} (G^-). The G^+ feature is associated with carbon atom vibrations along the nanotube axis (LO phonon mode) and its frequency ω_{G^+} is sensitive to charge transfer from dopant additions to SWNTs (up-shifts in ω_{G^+} for acceptors, and downshifts for donors as in graphite intercalation compounds (GICs) [65,66]). The G^- feature, in contrast, is associated

[7] SDS-wrapped SWNT samples consist of not only isolated SWNTs, but also contain some small bundles with several SWNTs. Thus a weaker bundle effect than for a thick bundle should be observed. Centrifugal separation (24 h, 20,000 G) of SDS-SWNT(1.0 $\mathrm{g\,cm}^{-3}$) dissolved in D_2O (1.3 $\mathrm{g\,cm}^{-3}$) increases the probability of producing isolated SDS–SWNT at the central region. The purity of the sample can be evaluated by Raman spectroscopy.

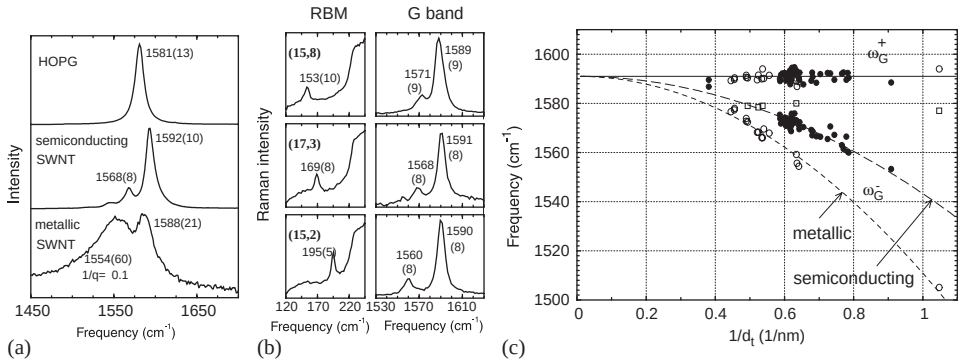

Fig. 14. (a) The *G*-band for highly oriented pyrolytic graphite (HOPG), one semiconducting SWNT and one metallic SWNT. (b) RBM and *G*-band Raman spectra for three semiconducting isolated SWNTs of the indicated (n, m) values. (c) Frequency vs. $1/d_t$ for the two most intense *G*-band features (ω_G^- and ω_G^+) from isolated SWNTs. [47].

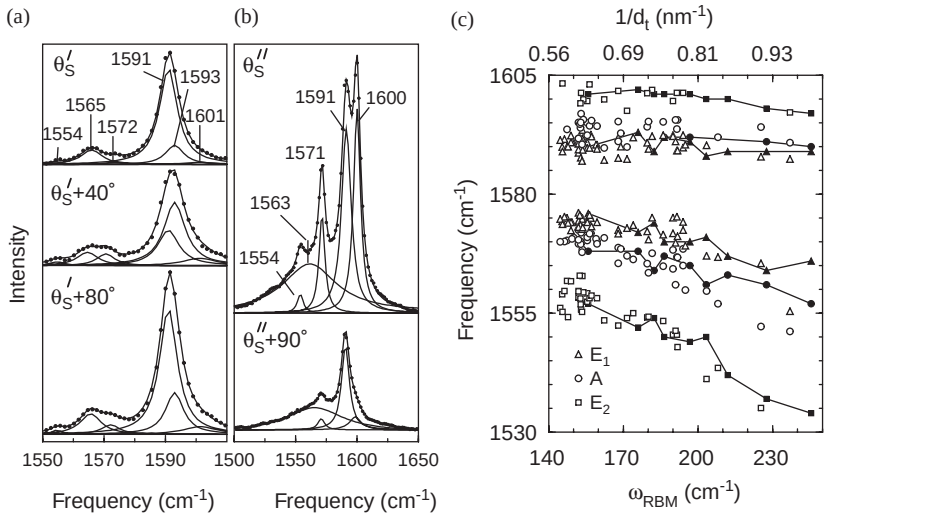

Fig. 15. Polarization scattering geometry dependence for the *G*-band from two isolated SWNTs (a) and (b) in resonance with $E_L = 2.41$ eV. The Lorentzian peak frequencies are in cm^{-1}. θ'_S and θ''_S are the initial angles between the light polarization and SWNT axis directions, not known a priori. (c) ω_G (open symbols) vs. ω_{RBM} (bottom axis) and $1/d_t$ (top axis) for semiconducting SWNTs. Experimental data are obtained with $E_L = 1.58$, 2.41 and 2.54 eV. The ω_G are clearly dependent on d_t, but there is no clear evidence for any ω_G dependence on E_L. The spectra with $\omega_{RBM} > 200\,cm^{-1}$ were obtained with $E_L = 1.58$ eV. Solid symbols connected by solid lines come from ab initio calculations [64] downshifted by 18, 12, 12, 7, 7, 11 cm^{-1} from the bottom to the top of the ab initio data, respectively [26].

with vibrations of carbon atoms along the circumferential direction of the SWNT (TO phonon), and its lineshape is highly sensitive to whether the SWNT is metallic (Breit–Wigner–Fano lineshape) or semiconducting (Lorentzian lineshape), as shown in Fig. 14(a) [67,68]. Charge transfer to SWNTs can lead to an intensity increase or decrease of the BWF feature [69,70].

Measurements on the G band at the single nanotube level show that the G-band is a first-order process [26,71], with the frequency ω_{G^+} essentially independent of d_t or chiral angle θ, while ω_{G^-} is dependent on d_t and whether the SWNT is metallic or semiconducting, but not on chiral angle θ [see Fig. 14(c)]. Such diameter-dependent measurements can only be done at the single nanotube level, and the results can be used along with measurements on other Raman features to corroborate (n, m) assignments carried out on the basis of the RBM feature (see Section 6.1.3) [3,26].

From the diameter dependence for the G band modes shown in Fig. 14(c), it is clear that the G band for large diameter carbon nanotubes is similar to the one peak G-band observed in graphite. This is actually the case for the G band for large diameter multi-wall carbon nanotubes (MWNTs), where a single peak at $1582\,\mathrm{cm}^{-1}$ is observed, just like in graphite (see Section 8).

6.2.2. Polarization analysis

A more careful analysis of the two G-band features shows that the G^+ and G^- features are both composed of three peaks of different symmetries. While the two most intense peaks (G^+ and G^-) at $\sim$ 1593 and $\sim$ $1567\,\mathrm{cm}^{-1}$, respectively, arise from phonons with A and E_1 symmetries, the smaller intensity features at $\sim$ 1526 and $\sim$ $1606\,\mathrm{cm}^{-1}$ are associated with E_2 symmetry phonons. Phonons with A, E_1 and E_2 symmetries can be distinguished from one another by their behavior in polarization-sensitive Raman experiments [25,26], as discussed in Section 4.2.4.

Fig. 15(a) shows three different G-band Raman spectra from a semiconducting SWNT, but with different directions for the incident light polarization, i.e., θ'_S, $\theta'_S + 40°$ and $\theta'_S + 80°$. Well-defined peaks associated with the G-band features are clearly observed, with different relative intensities for the different polarization geometries. From their relative intensities, we conclude that the spectrum for θ'_S corresponds to the $Y[ZZ]\bar{Y}$ scattering geometry (see Section 4.2.2), and we assign the peaks as follows: 1565 and $1591\,\mathrm{cm}^{-1} \rightarrow A$; 1572 and $1593\,\mathrm{cm}^{-1} \rightarrow E_1$; 1554 and $1601\,\mathrm{cm}^{-1} \rightarrow E_2$. This SWNT exhibits $\omega_{\mathrm{RBM}} = 180\,\mathrm{cm}^{-1}$ ($d_t = 1.38\,\mathrm{nm}$) [3].

Fig. 15(b) shows two G-band Raman spectra obtained from another semiconducting SWNT, and taken with incident light polarization directions θ''_S and $\theta''_S + 90°$. In this case, the spectrum at θ''_S is assigned as the $Y[XX]\bar{Y}$ scattering geometry, and the sharp peaks at 1554 and $1600\,\mathrm{cm}^{-1}$ are assigned as E_2 modes, while the 1571 and $1591\,\mathrm{cm}^{-1}$ peaks are assigned as unresolved $(A + E_1)$ modes, their relative intensities depending on the incident light polarization direction [26].

Analysis of the d_t dependence of the 6 G-band modes ($2A$, $2E_1$ and $2E_2$) for semiconducting SWNTs has been done at the single nanotube level [26] and the results agree quite well with ab initio calculations in the $1.0 < d_t < 2.0\,\mathrm{nm}$ diameter range [64], thus supporting the symmetry assignments. Fig. 15(c) plots the G-band mode frequencies for several semiconducting SWNTs in resonance with the incident laser light vs. the observed ω_{RBM} (bottom axis) and inverse nanotube diameter $1/d_t = \omega_{\mathrm{RBM}}/248$ (top axis) [3]. The solid symbols connected by solid lines come from ab initio calculations by Dubay et al. [64]. The G^- experimental data from semiconducting SWNTs can be better fit with $\omega_G = 1592 - C/d_t^{\beta}$, with $\beta = 1.4$, $C_A = 41.4\,\mathrm{cm}^{-1}\,\mathrm{nm}$, $C_{E_1} = 32.6\,\mathrm{cm}^{-1}\,\mathrm{nm}$, $C_{E_2} = 64.6\,\mathrm{cm}^{-1}\,\mathrm{nm}$. In Section 6.2.1, the G^- diameter dependence shown in Fig. 14(c) was fit with ($\beta = 2$ [47]) obtained using only one Lorentzian peak to fit the G^- feature in the unpolarized G-band spectra. Although the analysis in Fig. 14(c) is not fully correct, it is much simpler and can be easily used to characterize SWNT diameters from the G-band feature.

From these studies, we conclude that polarization analysis of the Raman spectra and a comparison with ab initio calculations are consistent with the observation of A, E_1 and E_2 symmetry modes in the G-band

for SWNTs. According to the resonance Raman selection rules discussed in Section 4.3, E_2 symmetry modes can only be observed for cross-polarized light in resonance with electronic transitions from the E_μ^{v} to $E_{\mu\pm1}^{\mathrm{c}}$ van Hove singularities (vHSs). Up to now, it has been well accepted that optical spectra (absorption, resonance Raman scattering, etc.) are dominated by absorption/emission of light polarized parallel to the tube axis because of the antenna effect [15,17]. In other words, only $E_{\mu\mu}$ vHSs in the joint density of states (JDOS) have been taken into account thus far when analyzing Raman and optical absorption spectra from SWNTs. It is shown in Fig. 15(b) that resonance Raman scattering for cross-polarized light involving the $E_{\mu,\mu\pm1}$ vHSs in the JDOS also needs to be taken into account when analyzing Raman spectra from isolated SWNTs. This important result implies that asymmetries between electronic levels above and below the Fermi level in SWNTs (related in a simplistic way to the overlap integral parameter s in the tight binding approximation) [15,17] can be obtained experimentally by studying the JDOS optically.[8]

7. Learning about carbon nanotubes from their double-resonance Raman features

7.1. Overview of double resonance spectral features

Although generally of weaker intensity than the first-order Raman features presented in Section 6, the second-order Raman spectra (either two-phonon or defect-induced) provide a large amount of important information about carbon nanotube electronic and vibrational properties that cannot be obtained by probing the first-order features. This is the central focus of the present section. Such an abundance of new information becomes accessible because the selection rules for the second-order features are relaxed with respect to the first-order features (see Section 6), thus making it possible to probe the interior of the Brillouin zone. The achievement of the double resonance condition (see Section 3.3), on one hand, makes the Raman signal strong enough to be easily detected, and, on the other hand, makes it possible to address specific points in the 2D Brillouin zone, since the double resonance process is strongly selective in phonon wave vector.

In Sections 3.3 and 3.4, the double resonance processes are discussed. Although the double resonance process gives rise to many peaks in the SWNT Raman spectra, the D and G' bands (see Fig. 10) are usually the two strongest second-order features and these are the features that have been studied in most detail. The physics related to these features is discussed in Sections 7.1–7.5, while in Sections 7.6 and 7.7 we review the smaller intensity double resonance features, namely the M-bands, the iTOLA feature, and the intermediate frequency modes, which have so far received little attention, but clearly are important effects that shed new light on novel aspects of nanotube physics.

Two double resonance features commonly found in the Raman spectra of SWNT bundles are the D-band feature (with ω_D at $\sim 1350\,\mathrm{cm}^{-1}$ for $E_{\mathrm{L}} = 2.41\,\mathrm{eV}$), stemming from the disorder-induced mode in graphite with the same name [16]), and its second harmonic, the G' band occurring at $\sim 2\omega_D$ [17]. In 2D graphite, the D-band originates from the iTO phonon branch [see Fig. 5(a)] close to the K point in the

[8] This asymmetry between valence and conduction band sublevel spacings cannot be studied by analyzing $E_{\mu\mu}$ transitions, because the expansion and contraction of energy differences between subbands in the valence and conduction bands cancel each other for $E_{\mu\mu}$ transitions. However, if $s \neq 0$ and if SWNT curvature effects are taken into account, then the optical transition energies $E_{\mu,\mu\pm1}$ and $E_{\mu\pm1,\mu}$ are no longer equal and measurement of these energy differences give the valence and conduction band asymmetries [6,8,72].

BZ. In nanotubes, both the D-band and the G'-band are sensitive to the SWNT diameter and chirality, since these features depend sensitively on how the 2D electronic and phonon structure is folded into a 1D structure (see Section 2). As a result, the D-band and G'-band in SWNTs can have much narrower spectral widths (less than $10\,\mathrm{cm}^{-1}$) [51] than in graphite (30–$50\,\mathrm{cm}^{-1}$).

Single nanotube measurements have confirmed that the D-band and G'-band for SWNTs are well described by a double resonance process as in graphite [18], but with special properties that arise from the van Hove singularities occurring in the electronic joint density of states for SWNTs [19,72–76]. Measurements of the D-band and the G'-band frequencies at the single nanotube level therefore provide unique information on the chirality and diameter dependence of ω_D and $\omega_{G'}$ that can be used to determine the magnitude of the trigonal warping effect in the electron and phonon dispersion relations of SWNTs, thereby providing information not readily available using other experimental techniques [15]. Because the dispersion is larger for the G'-band and because the G'-band is less sensitive to nanotube defects, many of the fundamental studies on the electronic and phonon structure of SWNTs have been done on the G'-band feature. In the next sections we discuss the physics about SWNTs and HOPG that is elucidated by the G'-band spectra.

7.2. Analysis of the G' band spectra

The dominant feature in the second-order Raman spectra in graphite and SWNTs is the G' band feature arising from a two-phonon, intervalley, second-order Raman scattering process. For a high-quality sample, the G' spectra are completely free from defect contributions, and the experimental G'-band signal can be comparable in intensity to the G band. The Raman spectra for the G'- band phonon energy region have been calculated in the context of a double resonance process, and considering both electron–photon and electron–phonon coupling for two phonon-emitting processes (see Section 4.4.2).

Let us discuss Fig. 9 again from an experimental point of view. Here we compare the calculated G' band spectra for several laser energies with experimental results for HOPG and G'-band spectra. The maximum G'-band intensity in the calculation is normalized to the experimental peak height. Fig. 9 shows that the calculated results reproduce the dispersive nature and spectral shape of the experimental peak around $2700\,\mathrm{cm}^{-1}$ very well. A small peak which is non-dispersive is also observed experimentally around $2450\,\mathrm{cm}^{-1}$. The calculation also shows the presence of a non-dispersive second-order phonon peak but the calculations predict its occurrence at a somewhat lower frequency region ($\sim 2350\,\mathrm{cm}^{-1}$). The calculation, however, indicates that this feature can be assigned to a non-dispersive second-order $q = 0$ intravalley Raman feature, and its intensity relative to the $2700\,\mathrm{cm}^{-1}$ peak intensity can be evaluated theoretically. Since the peak at $2450\,\mathrm{cm}^{-1}$ is much weaker than the $2700\,\mathrm{cm}^{-1}$ peak, a good quality sample and a long experimental observation time is required to observe the non-dispersive $2450\,\mathrm{cm}^{-1}$ peak experimentally [38].

7.3. SWNT electronic structure obtained by G'-band studies

In this section it is seen how studies on the $\omega_{G'}$ phonon frequencies in the Raman spectra provide unique information about the electronic structure of both semiconducting and metallic SWNTs. While the G'-band normally appears as a single peak in most graphitic materials, it sometimes appears (at the individual nanotube level) in the form of unusual two-peak structures for both semiconducting [73] and metallic [74] nanotubes. It should be noted that the G'-band doublet structure that is observed in 3D

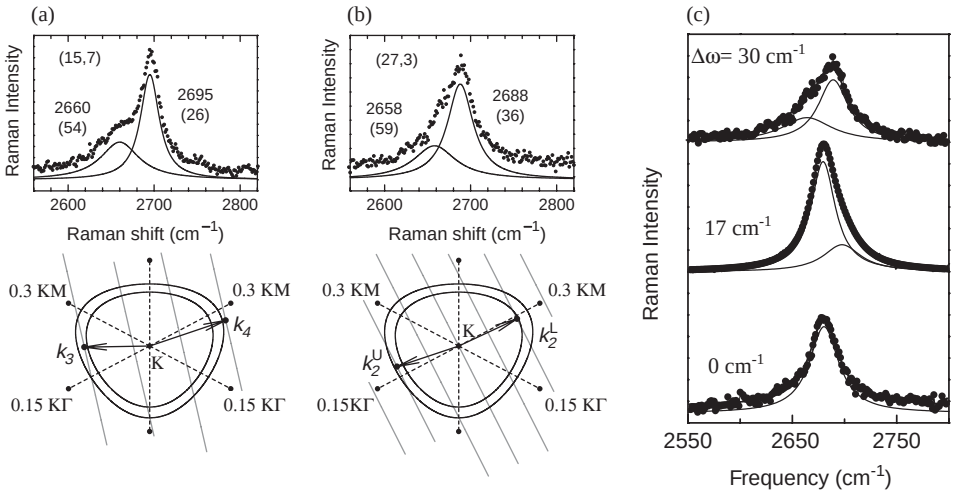

Fig. 16. The G'-band Raman features for (a) semiconducting (15, 7) and (b) metallic (27, 3) nanotubes show unusual two-peak structures, taken from Refs. [73,74], respectively. The *vicinity* of the K point in the unfolded Brillouin zone corresponding to each SWNT is shown below each spectrum, where the equi-energy contours for the incident $E_{\mathrm{L}} = 2.41\,\mathrm{eV}$ and the scattered $E_{\mathrm{L}} - E_{G'} = 2.08\,\mathrm{eV}$ light, together with the wave vectors for the resonant vHSs ($E_{33}^{\mathrm{S}} = 2.19\,\mathrm{eV}$, $E_{44}^{\mathrm{S}} = 2.51\,\mathrm{eV}$, for the (15,7) SWNT, and $E_{22}^{\mathrm{M(L)}} = 2.04\,\mathrm{eV}$, $E_{22}^{\mathrm{M(U)}} = 2.31\,\mathrm{eV}$ for the (27,3) SWNT), are also shown. (c) The G'-band Raman spectra for the isolated metallic (15,15), (19,10) and (27,3) SWNTs from the bottom to the top whose (n, m) indices are assigned by using their radial breathing mode properties [3].

graphitic materials is attributed to the interlayer coupling [77] and this mechanism does not apply to SWNTs. The two-peak G'-band Raman features observed from semiconducting and metallic isolated nanotubes are shown in Figs. 16(a) and (b), respectively, where the (n, m) indices for these nanotubes are assigned as (15,7) and (27,3) following the standard procedure [3]. The presence of two peaks in the G'-band Raman feature from semiconducting SWNTs indicates resonance with two different vHSs of the same nanotube, occurring independently for both the incident E_{L} and scattered $E_{\mathrm{L}} - E_{G'}$ photons (see Section 3.2) when the vHSs are sufficiently separated in energy (outside their respective resonance windows). The wave vectors corresponding to the resonance vHSs are shown in the unfolded 2D Brillouin zone of the graphene layer in Fig. 16 below the G'-band profiles. The use of cutting lines allows us to account simultaneously for both 1D wave vector conservation along the nanotube axis and wave function matching in the circumferential direction [78].

The two peaks in Figs. 16(a) and (b) can be associated with phonon modes corresponding to the wave vectors $\mathbf{q}_i = -2\mathbf{k}_i$, where $i = 3, 4$ labels the resonant electronic states for the semiconducting SWNTs, and $i = 2\mathrm{L}, 2\mathrm{U}$ labels these states for the metallic E_{22}^{M} vHSs. For the semiconducting SWNT Raman spectrum, the resonant wave vectors $\mathbf{k}_3$ and $\mathbf{k}_4$ have different magnitudes, with a difference of $k_4 - k_3 \simeq K_1/3$, resulting in twice the difference for the phonon wave vectors, $q_4 - q_3 \simeq 2K_1/3 = 4d_t/3$. Thus, for semiconducting SWNTs, the observed splitting of the G'-band Raman feature arises from the *phonon dispersion* $\omega_{\mathrm{ph}}(q)$ around the K point because the vHSs for E_{33}^{S} and E_{44}^{S} for the same SWNT occur at different energies and different resonant wave vectors k_3 and k_4, as in Fig. 16(a). In contrast, for the metallic nanotube shown in Fig. 16(b), the resonant wave vectors $\mathbf{k}_{2\mathrm{L}}$ and $\mathbf{k}_{2\mathrm{U}}$ have roughly

equal magnitudes but have opposite directions away from the K point, so that the splitting of the G'-band Raman feature for metallic nanotubes arises from the *anisotropy* of the phonon dispersion $\omega_{\mathrm{ph}}(q)$ around the K point, known as the phonon trigonal warping effect (see Section 7.4) [78]. The Raman effect thus provides a sensitive probe of the electronic trigonal warping effect for metallic SWNTs. Overall, the presence of two peaks in the double resonance Raman features of isolated carbon nanotubes is associated with quantum confinement effects expressed in terms of the cutting lines shown in Fig. 16. Therefore, the two-peak structure of the double resonance Raman features is a special property of SWNTs, that is not observed in 2D graphitic materials [see Fig. 3(a)].

These G'-band observations, are particularly useful for corroborating specific (n, m) assignments made by the RBM mode (see Section 6.1.3), as well as for corroborating the (n, m) assignment procedure itself [15]. The corresponding measurements for metallic SWNTs provide definitive information about the magnitude of the trigonal warping effect in the electronic structure of metallic SWNTs [74]. The G'-band spectra for metallic SWNTs in Fig. 16(c) are seen to have a different lineshape profile, depending on the chiral angle of the SWNT. From the bottom to the top of Fig. 16(c), the chiral angle θ decreases, going from 30° to 19.8° to 5.2° for the (15,15), (19,10), and (27,3) SWNTs, respectively, thereby increasing the trigonal warping-induced splitting $\Delta E_{22}^{\mathrm{M}}$ of the peaks for the E_{22}^{M} interband transition in the electronic joint density of states [1,35]. Firstly, the bottom spectrum, identified with the (15,15) nanotube, has only one peak at 2680 cm^{-1}. Secondly, a doublet with different $\omega_{G'}$ splittings appears for the chiral (19,10) and (27,3) nanotubes, the largest splitting being 30 cm^{-1} [see Fig. 16(c)]. A comparison between the G'-band properties in Fig. 16(c) and the calculated electronic structure shows that the splitting of the van Hove singularities due to the trigonal warping effect for the electronic dispersion relations $E(k)$ is properly reflected in the G'-band phonon spectra.

7.4. Phonon trigonal warping effect

The 1D structure of carbon nanotubes also leads to quantum confinement of the wave vectors for the phonon states. Since $\mathbf{q}_i = 2\mathbf{k}_i$ through the wave vector selectivity of the double resonance Raman process, not only is the Raman process selective of the magnitude of $\mathbf{q}$, but also of the direction of $\mathbf{q}$. This additional selectivity, arising from low dimensionality, allows us to measure $\omega(\mathbf{q})$ and thus to reconstruct the phonon dispersion relations of 2D graphite, by probing individual single-wall carbon nanotubes of different chiralities by resonance Raman spectroscopy, and using different laser excitation energies. This direction is chosen in SWNTs by selecting the chiral angle. In particular, the dependence of ω_D on chiral angle has been measured at the single nanotube level, yielding the anisotropy of $\omega_D(\mathbf{q})$, thereby providing a measure of the trigonal warping effect in the *phonon dispersion* relations for SWNTs about the hexagonal corner (K point) of the Brillouin zone of graphite.

Fig. 17(a) and (b) show the trigonal warping of the phonon dispersion relations for $\omega_D(\mathbf{q})$ around the K point of the 2D BZ, fitted to the experimental points shown by the dots. Fig. 17(c) shows the angular dependence of ω_D around the K point, for a given q value ($|q| = 0.24 K\Gamma$), where $K\Gamma$ here denotes the length of the phonon wave vector from the K to Γ points in the BZ. The phonon dispersion in Fig. 17(c) shows a measured frequency difference of $\Delta\omega_D = 24\,\mathrm{cm}^{-1}$ as the chiral angle θ is varied in the range $0° < \theta < 30°$. The trigonal warping effect for phonons increases by increasing the distance of the wave vector q from the K point [78]. Fig. 17(c) represents the first experimental measurement of the trigonal warping effect of phonons in either 2D graphite or in SWNTs.

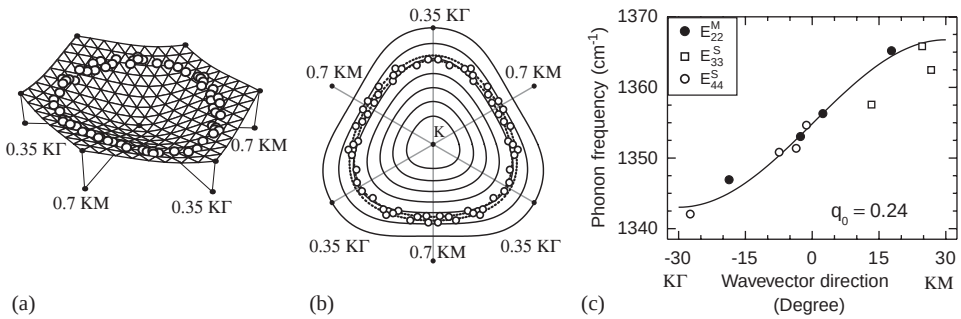

Fig. 17. (a) Phonon dispersion relations $\omega_{\mathrm{ph}}(\mathbf{q})$ around the K point of the 2D BZ of graphite fitted to the experimental points $\omega_D(\mathbf{q}_i)$ shown by dots. (b) Phonon equi-frequency contours (solid curves), and the experimental q-points (dots) from (a). (c) Dependence of $\omega_D(\mathbf{q})$ on the q-vector direction for a given q magnitude $q_0 = 0.24K\Gamma$, where $K\Gamma$ denotes the length of the vector from the K point to the Γ point. The frequency difference in ω_D for two different q-vector directions KM and $K\Gamma$ that differ by 60° [see (b)] is $\Delta\omega_D = 24\,\mathrm{cm}^{-1}$ [78].

7.5. Characterization of structural modifications of the nanotube sidewalls

Furthermore, changes in the D-band and G'-band Raman spectra can be used for materials characterization to probe and monitor structural modifications of the nanotube sidewalls that come from the introduction of defects and the attachment of different chemical species. The former effect can be probed through analysis of the disorder-induced Raman modes (e.g., the D-band shown in Fig. 10) and the latter through the upshifts/downshifts observed in the various Raman modes, such as in the G^+ band and the G' band due to charge transfer effects for acceptors/donors [69,79] (see Section 6.2.1).

Sample purity can also be investigated using the D/G band intensity ratio in the Raman spectra from SWNTs, in analogy to the characterization normally done in carbon-based materials generally [80]. However, further effort is needed to make this materials characterization method reliable and perhaps also sensitive to specific SWNT defects for the case of SWNTs. In the future, improved materials characterization will come from exploiting the unique properties of the electron and phonon density of states and of the electron–photon and electron–phonon matrix elements for SWNTs to identify intensity and lineshape effects associated with specific defects [80,81].

7.6. Overtones and combination modes above the G-band frequency

In general the observation of overtones and combination modes in condensed matter systems is rare because of dispersion effects which make these features too weak and broad to pick out from the noisy background. The double resonance process and the presence of van Hove singularities in SWNTs, however, allow such overtones and combination modes to be quite clearly observed, thereby providing new information about SWNT properties.

One set of overtone features that has received some attention is the M feature near $1750\,\mathrm{cm}^{-1}$ which is shown in Fig. 18(a), for SWNT bundles [45] and for several laser lines (E_{L}). This feature can be analyzed in terms of two components with frequencies ω_{M}^- and ω_{M}^+, where the lower frequency mode ω_{M}^- exhibits a weakly dispersive behavior (frequency ω_{M}^- shifting down by $\sim 30\,\mathrm{cm}^{-1}$ as E_{L} is varied from 1.58 to 2.71 eV), while the upper feature frequency ω_{M}^+ is basically independent of E_{L}. The two features

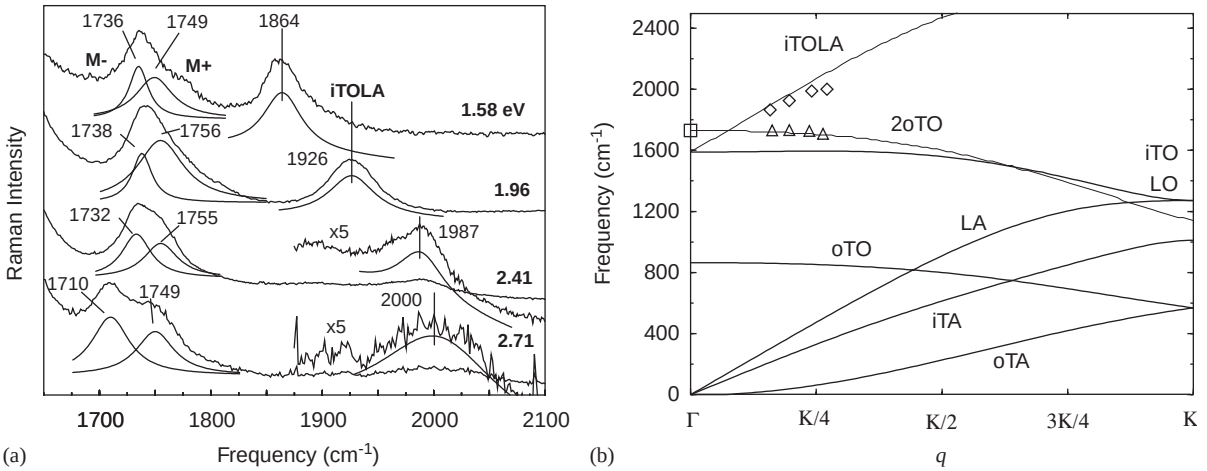

Fig. 18. (a) Lorentzian fits of the Raman spectra taken at several E_L values for the M-bands near 1750 cm^{-1} and the highly dispersive iTOLA feature observed at 1950 cm^{-1} in SWNT bundles [45,82]. Peak frequencies (cm^{-1}) and E_L values (eV) are displayed. (b) Phonon dispersion for 2D graphite along the Γ–K direction, including the dispersion for 2oTO and iTO+LA. Squares, up-triangles and diamonds denote experimental values for the M ($q = 0$ and $q = 2k$) and iTOLA ($q = 2k$) bands, which are here placed on the phonon dispersion curves in accordance with double resonance theory [45].

near 1750 cm^{-1} (M band) are attributed to overtones of the out-of-plane (oTO), infrared-active mode at 867 cm^{-1} in graphite. Here the M^+ feature is identified with an intravalley $q = 0$ scattering process, and the M^- with an intervalley $q = 2k$ process [see Fig. 18(b)]. A downshift of about 20 cm^{-1} occurs for both the M^+ and M^--band features in SWNTs relative to 2D graphite because of diameter-dependent curvature effects (see Section 5.3) [45,46,82]. The second-order M-band features are also interesting as an example of an overtone mode near $q = 0$ whose fundamental (oTO) is not Raman-active [81] (but is IR active) in the first-order spectrum of graphite, but can be observed in the second-order spectrum of graphite through the double resonance process. The M-band modes are further enhanced in SWNTs by van Hove singularity effects, and by symmetry-breaking effects associated with SWNT curvature.

The higher-frequency iTOLA combination mode is highly dispersive and upshifts from 1864 to 2000 cm^{-1} as E_L varies from 1.58 to 2.71 eV [45]. This feature can be assigned as a combination mode not seen in graphite, but enhanced by the $q = 2k$ double resonance process [22]. To account for the large observed dispersion with E_L, this so-called iTOLA band is attributed to a combination of two intravalley phonons, one from the in-plane transverse optical branch (iTO) and the second phonon from the longitudinal acoustic (LA) branch, iTO+LA, where the acoustic LA phonon is responsible for the large dispersion that is observed experimentally [45]. The experimental dispersion of this feature is shown in Fig. 18(a), while Fig. 18(b) shows the relation of this mode dispersion to phonon branches in 2D graphite.

7.7. Combination modes with frequencies between the RBM and G-band

Resonance Raman spectroscopy with an energy tunable laser excitation system has been used to analyze the Raman features for SWNTs appearing in the spectral region between 600 and 1100 cm^{-1} which we call intermediate frequency modes (IFMs) since their frequencies lie between ω_{RBM} and ω_G [83]. The

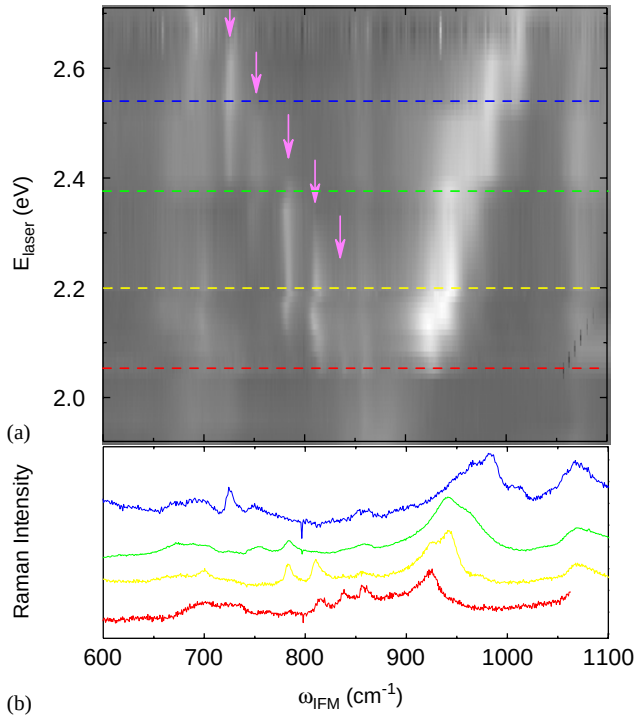

Fig. 19. (a) 2D plot for the E_{L} dependence for the Raman spectra of SWNT bundles in the intermediate frequency mode (IFM) range. The illuminated areas indicate high Raman intensity. Arrows point to five well-defined $\omega_{\mathrm{IFM}}^{-}$ features. (b) IFM Raman spectra with $E_{\mathrm{L}} = 2.05$(top), 2.20, 2.34, and 2.54 eV (bottom) [40].

"dispersive" IFMs observed at several laser energies are attributed to combination modes which relate to the double resonance process. Further additional quantum confinement of phonon modes is observed (see Fig. 19) by using a tunable laser system and these quantum-confined IFMs are not dispersive [40].

Fig. 19(a) plots the E_{L} dependence of the IFM features. This figure was constructed by taking IFM spectra obtained with 22 different E_{L} values between 1.92 and 2.71 eV, and represents results that would be seen by a continuously tunable laser. The illuminated areas in Fig. 19(a) indicate Raman peaks. The IFM Raman spectra obtained with $E_{\mathrm{L}} = 2.05$, 2.20, 2.34, and 2.54 eV are shown in Fig. 19(b), and these exhibit broad features at about 700, 860 and 1070 cm^{-1}, which are observed for every E_{L} and are basically not dispersive. Other features with a dispersive behavior (i.e., frequencies changing with changing E_{L}) are also found in these spectra.

In the 2D graphite parent material (see Fig. 5), the IFM spectral region is composed of an out-of-plane optical branch (here labeled O, with $\omega_{\mathrm{O}}(q=0) \sim 860\,\mathrm{cm}^{-1}$ for the oTO mode) and by acoustic branches (here labeled A) [1]. In a second-order scattering process, these modes can become Raman active, and the sum and difference of phonon frequencies can be observed. Such an effect is common in molecular spectroscopy, but is very unusual for solid-state spectroscopy, where too many combinations are possible, and the averaging over many wave vector-allowed processes gives rise to just a broad background rather than observable peaks with well-defined frequencies. The IFMs can be related to the combination of two phonons that originate from a zone-folding procedure of two 2D phonon branches, one optical (O) and one

acoustic (A). The O frequency ω_O phonon exhibits a weak negative dispersion, whereas the A frequency ω_A mode exhibits a stronger positive dispersion related to the high speed of sound in 2D graphite [1]. The sum $\omega^{+}_{IFM} = \omega_O + \omega_A$ (creation of two phonons) and the difference $\omega^{-}_{IFM} = \omega_O - \omega_A$ (creation of an O phonon and the annihilation of an A phonon) give rise to positively and negatively dispersive IFMs in Fig. 19(a), respectively.

Interestingly, the use of a tunable system and 22 different laser lines, with a small energy spacing between them, brings into focus a new and very unusual effect for Raman spectroscopy. When E_L is varied, individual Raman peaks first increase and then decrease in intensity, while remaining approximately constant in frequency. This behavior can be seen clearly by observing some of the well-resolved sharp peaks [see arrows in Fig. 19(a)]. The dispersive behavior is not monotonic, as observed for many features in graphite-like materials due to energy-selective double-resonance Raman scattering processes [18,22], but it rather occurs in "steps". We thus refer to this new effect illustrated in Fig. 19(a) as a "step-like dispersive behavior".

It is important to note that the appearance and disappearance of peaks in the IFM region cannot be explained by the well-known single-resonance Raman effect, as is observed for first-order single resonance modes in SWNTs, such as the radial breathing modes (RBMs) discussed in Section 6.1. Considering the d_t distribution ($d_t = 1.5 \pm 0.3$ nm) of the SWNT sample and the E_L values that were used, resonance with mostly the E^S_{33} and E^S_{44} electronic vHSs for semiconducting SWNTs can be achieved (see Fig. 4). More than 50 different semiconducting SWNTs have their E^S_{33} and E^S_{44} energies within this experimental E_L range, which means that the first-order single resonance RBM spectra should be composed of about 50 different RBM peaks. When looking at Fig. 19(a), it is clear that a very small number of IFM modes are observed experimentally [e.g., only 5 peaks, each jumping to lower frequencies in steps, as E_L is increased—see arrows in Fig. 19(a)]. Therefore, the IFM features cannot be explained on the basis of a first-order single resonance process.

The step-like dispersive intermediate frequency features are observed as sharp peaks associated with the combination of optic and acoustic-like modes, exhibiting a step-like dispersive frequency behavior with changing excitation laser energy, as shown in Fig. 19(a). The reason why only a small number of SWNTs exhibit IFMs is the highly selective process, a turn on/off effect in the scattering process controlled by the SWNT 1D structure were linear and angular momentum conservation for scattering of electrons by phonons, which are both confined into vHSs states, is highly selective. Further analysis shows that Raman signals are only possible for $\mathrm{mod}(2n + m, 3) = 1$ carbon nanotubes with low chiral angles ($\theta \sim 0°$). This additional symmetry constraint gives rise to special scattering selection rules that can only occur in low-dimensional materials [40].

8. Multi-wall carbon nanotubes—MWNTs

Because of the large diameter of the outer tubes for typical multi-wall carbon nanotubes (MWNTs) and because MWNTs contain an ensemble of carbon nanotubes with diameters ranging from small to very large, most of the characteristic differences that distinguish the Raman spectra in SWNTs from the spectra for graphite are not so evident in MWNTs. For example, the RBM Raman feature associated with a small diameter inner tube (less than 2 nm) can sometimes be observed when a good resonance condition is established [84,85], but this is not the usual result, since the RBM signal from large diameter tubes is usually too weak to be observable and the ensemble average of inner tube diameter broadens the

signal. However, when we use hydrogen gas in the arc discharge method, we can get a very thin innermost nanotube within a MWNT, even less than 1 nm in diameter [86], and in this case we can clearly observe strong RBM peaks in the Raman spectra at the isolated MWNT level.

Whereas the $G^+ - G^-$ splitting is large for small diameter SWNT tubes (see Section 6.2), the corresponding splitting of the G band in MWNTs is both small in intensity and smeared out due to the effect of the diameter distribution within the individual MWNTs, and because of the variation between different tubes in an ensemble of MWNTs in typical experimental samples. Therefore the G-band feature predominantly exhibits a weakly asymmetric characteristic lineshape, with a peak appearing close to the graphite frequency of 1582 cm^{-1} [87]. However for isolated MWNTs that contain very small diameter innermost tubes (prepared in the presence of hydrogen gas using the arc discharge method), it is possible to observe multiple G-band splitting effects even more clearly than for SWNTs [88], and this is because environmental effects (Section 6.1.4) become relatively small for the innermost nanotube in a MWNT relative to the interactions occurring between SWNTs and different environments. The Raman spectroscopy of MWNTs has not been well investigated up to now. Thus some new features observed only in MWNT might be expected.

A DWNT (double wall carbon nanotube) can be considered to be a kind of MWNT for which the interlayer interaction is generally considered to be turbostratic between the inner and outer nanotubes. More detailed Raman studies of DWNTs have, however, been carried out [89]. But for armchair–armchair DWNTs, some commensurate structure can be expected. In this case, the splitting of the G'-band which is observed in 3D graphite could be seen. Another novel direction for future exploration is the small RBM linewidths (down to 0.25 cm^{-1}) occurring for the inner wall tube within an isolated DWMT [52]. Thus we can conclude that many exciting research opportunities remain to be explored in MWNTs.

9. Summary and future directions

In this article we review the resonance Raman spectroscopy (RRS) of SWNTs and show how to use RRS to characterize SWNT samples using the many features observed in the rich RRS spectra. In particular, we show how the electronic and phonon properties of SWNTs can be investigated by using the strict resonance[9] conditions for many individual (n, m) SWNTs. Here we use the 1D property that the density of states (or joint density of states for optical transitions) for both electrons and phonons becomes singular $[(E - E_0)^{-1/2}]$, and this singularity is known as the van Hove singularity (vHS). Thus we can see optical transitions experimentally as a sharp energy "level" coming from a vHS with a width of $\sim$ 10 meV, even though the transition occurs over a continuous energy band. Since the vHS energy positions of each SWNT are different from one another, we can interpret Raman or absorption/emission spectra from a SWNT bundle sample by specifying the energy of the vHSs of each (n, m) SWNT. The Kataura plot (E_{ii} vs. d_t) is useful for assigning the (n, m) indices of individual SWNTs. From the RBM frequency which is inversely proportional to d_t (for example $\omega_{\mathrm{RBM}} = 248/d_t$ cm^{-1}), we can estimate the diameter d_t for individual SWNTs in resonance with the laser excitation energy E_{L}.

Both the resonance condition and the 1D vHS singularity contribute to enhancing the Raman intensity by up to 5 orders of magnitude. Such conditions enables us to observe single-molecule (SWNT) spectroscopy.

[9] Strict resonance is defined by the fact that the energy separation between the initial and final states of the transition exactly matches the excitation laser energy.

Generally, the resonance condition works at non-singular, continuous energy band states, too, but the signal from an individual SWNT is too small to observe unless E_L is in resonance with a 1D vHS. An important point to address here is that the vHS energy occurs at a k point in the 1D energy dispersion where the energy dispersion relation of electrons or phonons is flat. Thus we can investigate the solid-state properties of an isolated SWNT by RRS studies. Electron–photon and electron–phonon interaction matrix elements are unique in graphite because of the linear energy dispersion relation $E(k)$ near the Fermi energy, and for this reason these matrix elements also have unique properties for SWNTs. For example, a node is predicted for the photoluminescence intensity as a function of k. By investigating many SWNTs with different diameters and chiralities, we can probe the solid-state properties over the entire BZ of 2D graphite.

A second-order Raman process consists of (1) either a one-phonon + one-elastic scattering process, or a (2) two-phonon scattering process. Many weak Raman features can be assigned to specific second-order scattered processes according to their frequencies and their frequency dispersions with E_L. These weak second-order Raman features are rich in information about the electronic and vibrational structure of the SWNTs that cannot be probed from the first-order Raman features.

There are a number of parameters that can be probed by resonance Raman measurements: (1) (n, m) values, diameter and chirality, (2) laser energy, (3) polarization of light, (4) sample orientation relative to the polarization, (5) incident or scattered resonance, (6) Stokes and anti-Stokes Raman spectra, (7) laser power and temperature, (8) number of defects, (9) bundled or isolated, (10) environmental factors, including freely suspended SWNTs, substrates, wrapping agents, adsorbed species, whether in solution or in bundles, etc. Raman spectroscopy is very flexible for use, and is easy to handle at ambient pressure and room temperature. Micro-Raman spectroscopy has thus become a standard tool for characterizing nanotubes and nano-materials.

In single nanotube spectroscopy, all Raman peaks come from the same SWNT, so that the total Raman spectra contains a wealth of information which needs to be interpreted for self-consistency. Since the one-phonon + one-elastic Raman scattering process is closely related to defect scattering, we can estimate the sample quality by analyzing appropriate second-order spectral features such as the D-band. The relative intensity (or absolute intensity) of Raman spectra can be calculated, by including electron–photon and electron–phonon interactions as a function of (n, m), E_L, to yield detailed information about the effect on the spectra of specific defects and environmental conditions, and such information will be important in the future for sorting out the many discrepancies now in the literature arising from Raman spectra taken on SWNT samples under different experimental conditions, with different diameter distributions, and exposed to different environmental conditions.

It can be expected that future Raman studies will further explore the $2n + m$ family effects found experimentally for small diameter SWNTs [10,60,90] in an effort to develop a theoretical basis for the experimentally observed family behavior. This will be necessary for gaining a more detailed appreciation of the wealth of information provided by the rich spectra observed in resonance Raman spectroscopy, especially for small diameter SWNTs at the single nanotube level. Here RRS studies on individual freely suspended SWNTs of small diameter using polarized light are likely to be especially informative in view of theoretical developments. So far we have considered the optical processes and scattering for an electron. However for smaller diameter nanotubes (less than 1 nm), excitonic effects are expected to become more important and must be considered in detail, though for relatively large SWNTs, excitonic effects can be handled by using fitting parameters within the tight binding approximation. A detailed theoretical analysis to include excitonic effects will be needed to cover a large range of nanotube diameters.

Experimental studies using light polarized normal to the nanotube axis will be highly informative in verifying theoretical predictions regarding selection rules and relative intensities of the various Raman features as they appear under different scattering geometries. Such polarization studies will also allow quantitative measurements to be made of the anisotropy of the subband energies in the valence and conduction bands as a function of tube diameter, chiral angle, and whether the tube is metallic (MOD0), or semiconducting MOD1, or semiconducting MOD2 relative to the [MOD$(2n+m)$, 3] family structure. Experimental studies of the handedness of SWNTs by RRS under circular polarized light will be another fruitful direction for future studies. Near-field RRS studies on individual SWNTs [91] to elucidate spatial variations along the SWNT length will provide a powerful tool to study Raman signatures associated with specific defects.

Acknowledgements

A.J acknowledges financial support by PRPq-UFMG, and the Instituto de Nanociências (Millennium Institute Program), CNPq, Brazil. R.S. acknowledges a Grant-in-Aid (No. 13440091) from the Ministry of Education, Japan. G.D and M.S.D. acknowledge support under NSF Grants DMR 04-05538, and INT 00-00408.

References

[1] R. Saito, G. Dresselhaus, M.S. Dresselhaus, Physical Properties of Carbon Nanotubes, Imperial College Press, London, 1998.
[2] M.S. Dresselhaus, G. Dresselhaus, Ph. Avouris, Springer Series in Topics in Applied Physics, vol. 80, Springer, Berlin, 2001.
[3] A. Jorio, R. Saito, J.H. Hafner, C.M. Lieber, M. Hunter, T. McClure, G. Dresselhaus, M.S. Dresselhaus, Structural (n, m) determination of isolated single-wall carbon nanotubes by resonant Raman scattering, Phys. Rev. Lett. 86 (2001) 1118–1121.
[4] M.S. Dresselhaus, G. Dresselhaus, P.C. Eklund, Science of Fullerenes and Carbon Nanotubes, Academic Press, New York, NY, San Diego, CA, 1996.
[5] M.S. Dresselhaus, G. Dresselhaus, R. Saito, Carbon fibers based on C_{60} and their symmetry, Phys. Rev. B 45 (1992) 6234.
[6] Ge.G. Samsonidze, A. Grüneis, R. Saito, A. Jorio, A.G. Souza Filho, G. Dresselhaus, M.S. Dresselhaus, Interband optical transitions in left- and right-handed single-wall carbon nanotubes, Phys. Rev. B 69 (2004) 205402-(1–11)
[7] R. Saito, M. Fujita, G. Dresselhaus, M.S. Dresselhaus, Electronic structure of chiral graphene tubules, Appl. Phys. Lett. 60 (1992) 2204–2206.
[8] Ge.G. Samsonidze, R. Saito, A. Jorio, M.A. Pimenta, A.G. Souza Filho, A. Grüneis, G. Dresselhaus, M.S. Dresselhaus, The concept of cutting lines in carbon nanotube science, J. Nanosci. Nanotechnol. 3 (2003) 431–458.
[9] S.J. Tans, M.H. Devoret, H. Dai, A. Thess, R.E. Smalley, L.J. Geerligs, C. Dekker, Individual single-wall carbon nanotubes as quantum wires, Nature (London) 386 (1997) 474–477.
[10] Ge.G. Samsonidze, et al., Appl. Phys. Lett. 85 (2004) 5703–5705.
[11] The unique geometric structure of the carbon nanotube system, where all different SWNTs are related to the simple hexagonal graphene sheet, is responsible for the observation of well defined geometrical patterns in spectroscopy experiments, as firstly shown by O'Connell et al. in Science 2002. The most general pattern is related to the MOD0, MOD1 and MOD2 SWNT types, that exhibit different E_{ii} dependence on chiral angle, as shown in the Kataura plot. There are different (n, m) combinations for the mod calculation, such as mod$(n-m, 3)$, mod$(2n+m, 3)$ and mod$(2m+n, 3)$, that lead to the three different MOD types, although MOD1 and MOD2 can be interchanged for the same (n, m) SWNT depending on the combination one chooses. We here use mod$(2n+m, 3)$ because the $2n+m$ families group SWNTs with

similar diameter and make clearly defined pattern in the Kataura plot. Hereafter we call MOD0, MOD1 and MOD2 the three SWNT *classes*, and the many $2n + m$ values number the SWNT *families*.

[12] H. Kataura, Y. Kumazawa, Y. Maniwa, I. Uemezu, S. Suzuki, Y. Ohtsuka, Y. Achiba, Optical properties of single-wall carbon nanotubes, Synt. Met. 103 (1999) 2555.

[13] A. Jorio, M.A. Pimenta, A.G. Souza Filho, R. Saito, G. Dresselhaus, M.S. Dresselhaus, Characterizing carbon nanotube samples with resonance Raman scattering, New J. Phys. 5 (2003) 1.1–1.17.

[14] J. Maultzsch, S. Reich, C. Thomsen, H. Requardt, P. Ordejon, Phonon dispersion in graphite, Phys. Rev. Lett. 92 (2004) 075501.

[15] M.S. Dresselhaus, G. Dresselhaus, A. Jorio, A.G. Souza Filho, R. Saito, Raman spectroscopy on isolated single wall carbon nanotubes, Carbon 40 (2002) 2043–2061.

[16] F. Tuinstra, J.L. Koenig, Raman scattering in disordered graphite, J. Phys. Chem. 53 (1970) 1126.

[17] M.S. Dresselhaus, P.C. Eklund, Phonons in carbon nanotubes, Adv. Phys. 49 (2000) 705–814.

[18] C. Thomsen, S. Reich, Double resonant Raman scattering in graphite, Phys. Rev. Lett. 85 (2000) 5214.

[19] J. Kürti, V. Zólyomi, A. Grüneis, H. Kuzmany, Double resonant Raman phenomena enhanced by van Hove singularities in single-wall carbon nanotubes, Phys. Rev. B 65 (2002) 165433(1–9).

[20] M. Cardona, Topics in Applied Physics, vol. 50, pp. 19–176 (Chapter 2).

[21] R. Saito, A. Grüneis, Ge.G. Samsonidze, V.W. Brar, G. Dresselhaus, M.S. Dresselhaus, A. Jorio, L.G. Cançado, C. Fantini, M.A. Pimenta, A.G. Souza Filho, Double resonance Raman spectroscopy of single wall carbon nanotubes, New J. Phys. 5 (2003) 157.1–157.15.

[22] R. Saito, A. Jorio, A.G. Souza Filho, G. Dresselhaus, M.S. Dresselhaus, M.A. Pimenta, Probing phonon dispersion relations of graphite by double resonance Raman scattering, Phys. Rev. Lett. 88 (2002) 027401.

[23] L.G. Cançado, M.A. Pimenta, R. Saito, A. Jorio, L.O. Ladeira, A. Grüneis, A.G. Souza Filho, G. Dresselhaus, M.S. Dresselhaus, Stokes and anti-Stokes double resonance Raman scattering in two-dimensional graphite, Phys. Rev. B 66 (2002) 035415.

[24] R. M. Martin, L. M. Falicov, Topics in Applied Physics, vol. 8, pp. 79–145 (Chapter 3).

[25] A. Jorio, G. Dresselhaus, M.S. Dresselhaus, M. Souza, M.S.S. Dantas, M.A. Pimenta, A.M. Rao, R. Saito, C. Liu, H.M. Cheng, Polarized Raman study of single-wall semiconducting carbon nanotubes, Phys. Rev. Lett. 85 (2000) 2617–2620.

[26] A. Jorio, M.A. Pimenta, A.G. Souza Filho, Ge.G. Samsonidze, A.K. Swan, M.S. Ünlü, B.B. Goldberg, R. Saito, G. Dresselhaus, M.S. Dresselhaus, Resonance Raman spectra of carbon nanotubes by cross-polarized light, Phys. Rev. Lett. 90 (2003) 107403.

[27] A. Grüneis, R. Saito, J. Jiang, Ge.G. Samsonidze, M.A. Pimenta, A. Jorio, A.G. Souza Filho, G. Dresselhaus, M.S. Dresselhaus, Resonance Raman spectra of carbon nanotube bundles observed by perpendicularly polarized light, Chem. Phys. Lett. 387 (2004) 301–306.

[28] G.S. Chou, H.B. Ribeiro, E. Barros, A.P. Santos, D. Nazich, Ge.G. Samsonidze, C. Fantini, M.A. Pimenta, A. Jorio, F. Plentz Filho, M.S. Dresselhaus, G. Dresselhaus, R. Saito, M. Zheng, G.B. Onoa, E.D. Semke, A.K. Swan, M.S. Ünlü, B.B. Goldberg, Optical measurements of DNA wrapped carbon nanotube hybrids, unpublished.

[29] A. Grüneis, R. Saito, Ge.G. Samsonidze, T. Kimura, M.A. Pimenta, A. Jorio, A.G. Souza Filho, G. Dresselhaus, M.S. Dresselhaus, Inhomogeneous optical absorption around the K point in graphite and carbon nanotubes, Phys. Rev. B 67 (2003) 165402-1–165402-7.

[30] J. Jiang, R. Saito, A. Grüneis, G. Dresselhaus, M.S. Dresselhaus, Optical absorption matrix elements in single-wall carbon nanotube, Phys. Rev. B.

[31] L.G. Cançado, M.A. Pimenta, R.A. Neves, G. Medeiros-Ribeiro, T. Enoki, Y. Kobayashi, K. Takai, K. Fukui, M.S. Dresselhaus, R. Saito, A. Jorio, Anisotropy in the Raman spectra of nanographite ribbons, Phys. Rev. Lett. 93 (2004) 047403.

[32] H. Ajiki, T. Ando, Aharonov–Bohm effect in carbon nanotubes, Physica B 201 (1994) 349.

[33] H. Ajiki, T. Ando, Carbon nanotubes: optical absorption in Aharonov–Bohm flux, Jpn. J. Appl. Phys. Suppl. 34 (1) (1995) 107–109.

[34] M.J. O'Connell, S.M. Bachilo, X.B. Huffman, V.C. Moore, M.S. Strano, E.H. Haroz, K.L. Rialon, P.J. Boul, W.H. Noon, C. Kittrell, J. Ma, R.H. Hauge, R.B. Weisman, R.E. Smalley, Band gap fluorescence from individual single walled carbon nanotubes, Science 297 (2002) 593–596.

[35] R. Saito, G. Dresselhaus, M.S. Dresselhaus, Trigonal warping effect of carbon nanotubes, Phys. Rev. B 61 (2000) 2981–2990.

[36] Y. Miyauchi, S. Chiashi, Y. Murakami, Y. Hayashida, S. Maruyama, Fluorescence spectroscopy of single-walled carbon nanotubes synthesized from alcohol, Chem. Phys. Lett. 387 (2004) 198–203.
[37] R. Saito, A. Jorio, J.H. Hafner, C.M. Lieber, M. Hunter, T. McClure, G. Dresselhaus, M.S. Dresselhaus, Chirality-dependent G-band Raman intensity of carbon nanotubes, Phys. Rev. B 64 (2001) 085312–085319.
[38] T. Shimada, T. Sugai, C. Fantini, M. Souza, L.G. Cançado, A. Jorio, M.A. Pimenta, R. Saito, A. Grüneis, G. Dresselhaus, M.S. Dresselhaus, Y. Ohno, T. Mizutani, H. Shinohara, Origin of the 2450 cm^{-1} Raman bands in HOPG, single-wall and double-wall carbon nanotubes. Carbon (2005) in press.
[39] G. Moos, R. Fasel, T. Hertel, Temperature dependence of electron-to-lattice energy transfer in single-wall carbon nanotube bundles, J. Nanosci. Nanotechnol. 3 (2003) 145–149.
[40] C. Fantini, A. Jorio, M. Souza, L.O. Ladeira, M.A. Pimenta, G. Souza Filho, R. Saito, Ge.G. Samsonidze, G. Dresselhaus, M.S. Dresselhaus, Phys. Rev. Lett. 93 (2004) 087401.
[41] J.H. Hafner, C.L. Cheung, T.H. Oosterkamp, C.M. Lieber, High yield fabrication of single-walled nanotube probe tips for atomic force microscopy, J. Phys. Chem. B 105 (2001) 743.
[42] P. Corio, P.S. Santos, M.A. Pimenta, M.S. Dresselhaus, Evolution of the molecular structure of metallic and semiconducting carbon nanotubes under laser irradiation, Chem. Phys. Lett. 360 (2002) 557–564.
[43] S. Berber, Y.-K. Kwon, D. Tománek, Unusually high thermal conductivity of carbon nanotubes, Phys. Rev. Lett. 84 (2000) 4613.
[44] C. Fantini, et al., Phys. Rev. Lett. 93 (2004) 147406.
[45] V.W. Brar, Ge.G. Samsonidze, G. Dresselhaus, M.S. Dresselhaus, R. Saito, A.K. Swan, M.S. Ünlü, B.B. Goldberg, A.G. Souza Filho, A. Jorio, Second-order harmonic and combination modes in graphite single-wall carbon nanotube bundles and isolated single-wall carbon nanotubes, Phys. Rev. B 66 (2002) 155418.
[46] A.G. Souza Filho, A. Jorio, Ge.G. Samsonidze, G. Dresselhaus, M.A. Pimenta, M.S. Dresselhaus, A.K. Swan, M.S. Ünlü, B.B. Goldberg, R. Saito, Competing spring constant versus double resonance effects on the properties of dispersive modes in isolated single wall carbon nanotubes, Phys. Rev. B 67 (2003) 035427(1–7).
[47] A. Jorio, A.G. Souza Filho, G. Dresselhaus, M.S. Dresselhaus, A.K. Swan, M.S. Ünlü, B. Goldberg, M.A. Pimenta, J.H. Hafner, C.M. Lieber, R. Saito, G-band resonant Raman study of 62 isolated single wall carbon nanotubes, Phys. Rev. B 65 (2002) 155412.
[48] M. Milnera, J. Kürti, M. Hulman, H. Kuzmany, Periodic resonance excitation and intertube interaction from quasi-continuous distributed helicities in single-wall carbon nanotubes, Phys. Rev. Lett. 84 (2000) 1324–1327.
[49] A.G. Souza Filho, S.G. Chou, Ge.G. Samsonidze, G. Dresselhaus, M.S. Dresselhaus, Lei An, J. Liu, Anna K. Swan, M.S. Ünlü, B.B. Goldberg, A. Jorio, A. Grüneis, R. Saito, Stokes and anti-Stokes Raman spectra of small diameter isolated carbon nanotubes, Phys. Rev. B 69 (2004) 115428.
[50] J. Kürti, V. Zólyomi, M. Kertesz, G.Y. Sun, The geometry and the radial breathing mode of carbon nanotubes: beyond the ideal behaviour, New J. Phys. 5 (2003) 125.
[51] A. Jorio, C. Fantini, M.S.S. Dantas, M.A. Pimenta, A.G. Souza Filho, Ge.G. Samsonidze, V.W. Brar, G. Dresselhaus, M.S. Dresselhaus, A.K. Swan, M.S. Ünlü, B.B. Goldberg, R. Saito, Linewidth of the Raman features of individual single-wall carbon nanotubes, Phys. Rev. B 66 (2002) 115411.
[52] R. Pfeiffer, H. Kuzmany, Ch. Schaman, T. Pichler, H. Kataura, Y. Achiba, J. Kürti, V. Zólyomi, Unusual high degree of unperturbed environment in the interior of single-wall carbon nanotubes, Phys. Rev. Lett. 90 (2003) 225501.
[53] Ge.G. Samsonidze, S.G. Chou, A.P. Santos, A. Selbst, M.S. Dresselhaus, A.K. Swan, M.S. Ünlü, B.B. Goldberg, D. Chattopadhyay, S.N. Kim, F. Papadimitrakopoulos, Quantitative evaluation of the octadecylamine-assisted bulk separation of semiconducting and metallic single wall carbon nanotubes by resonance Raman spectroscopy, Appl. Phys. Lett. 85 (2004) 1006–1008.
[54] A. Jorio, A.G. Souza Filho, G. Dresselhaus, M.S. Dresselhaus, R. Saito, J.H. Hafner, C.M. Lieber, F.M. Matinaga, M.S.S. Dantas, M.A. Pimenta, Joint density of electronic states for one isolated single-wall carbon nanotube studied by resonant Raman scattering, Phys. Rev. B 63 (2001) 245416-(1–4).
[55] A.G. Souza Filho, A. Jorio, J.H. Hafner, C.M. Lieber, R. Saito, M.A. Pimenta, G. Dresselhaus, M.S. Dresselhaus, Electronic transition energy E_{ii} for an isolated (n, m) single-wall carbon nanotube obtained by anti-Stokes/Stokes resonant Raman intensity ratio, Phys. Rev. B 63 (2001) 241404R (1–4).
[56] M.S. Dresselhaus, G. Dresselhaus, A. Jorio, A.G. Souza Filho, Ge.G. Samsonidze, R. Saito, Science and applications of single nanotube Raman spectroscopy, J. Nanosci. Nanotechnol. 3 (2003) 19–37.

[57] S.M. Bachilo, M.S. Strano, C. Kittrell, R.H. Hauge, R.E. Smalley, R.B. Weisman, Structure-assigned optical spectra of single walled carbon nanotubes, Science 298 (2002) 2361–2366.
[58] HiPco nanotubes denote bundles of SWNTs prepared by a vapor phase process based on a CO feedstock [see O'Connell, et al., Science 297 (2002) 599]. Sonication is followed by use of a surfactant, sodium dodecyl sulfate (SDS), which wraps around individual SWNTs to disperse them and separate one SWNT from another.
[59] R.B. Weisman, S.M. Bachilo, Dependence of optical transition energies on structure for single-walled carbon nanotubes in aqueous suspension: an empirical Kataura plot, Nanoletters 3 (2003) 1235–1238.
[60] A. Jorio, et al., Phys. Rev. B 70 (2005) in press.
[61] A. Hagen, T. Hertel, Quantitative analysis of optical spectra from individual single-wall carbon nanotubes, Nanoletters 3 (2003) 383–388.
[62] H. Son, et al., Appl. Phys. Lett. 85 (2004) 4744–4746.
[63] The web site [http://www.fisica.ufmg.br/∼adojorio/] gives the (n, m) assignment thus obtained for both semiconducting and metallic nanotubes wrapped in SDS.
[64] O. Dubay, G. Kresse, H. Kuzmany, Accurate density functional calculations for the phonon dispersion relations of graphite layer and carbon nanotubes, Phys. Rev. Lett. 88 (2002) 235506 (1–4).
[65] M.S. Dresselhaus, G. Dresselhaus, Intercalation compounds of graphite, Adv. Phys. 30 (1981) 139–326 (see also 50 (2002) 1–186).
[66] T. Enoki, M. Endo, M. Suzuki, Graphite Intercalation Compounds and Applications, Oxford University Press, New York, 2003.
[67] M.A. Pimenta, A. Marucci, S. Empedocles, M. Bawendi, E.B. Hanlon, A.M. Rao, P.C. Eklund, R.E. Smalley, G. Dresselhaus, M.S. Dresselhaus, Raman modes of metallic carbon nanotubes, Phys. Rev. B Rapid 58 (1998) R16016–R16019.
[68] S.D.M. Brown, A. Jorio, P. Corio, M.S. Dresselhaus, G. Dresselhaus, R. Saito, K. Kneipp, Origin of the Breit–Wigner–Fano lineshape of the tangential G-band feature of metallic carbon nanotubes, Phys. Rev. B 63 (2001) 155414.
[69] P. Corio, P.S. Santos, V.W. Brar, Ge.G. Samsonidze, S.G. Chou, M.S. Dresselhaus, Potential dependent surface Raman spectroscopy of single wall carbon nanotube films on platinum electrodes, Chem. Phys. Lett. 370 (2003) 675–682.
[70] P. Corio, A. Jorio, N. Demir, M.S. Dresselhaus, Spectro-electrochemical studies of SWNT films, Chem. Phys. Lett. 392 (2004) 396–402.
[71] M. Souza, A. Jorio, C. Fantini, B.R.A. Neves, M.A. Pimenta, R. Saito, A. Ismach, E. Joselevich, V.W. Brar, Ge.G. Samsonidze, G. Dresselhaus, M.S. Dresselhaus, Single and double resonance Raman *G*-band processes in carbon nanotubes, Phys. Rev. B 69 (2004) 241403.
[72] V. Zólyomi, et al., Phys. Rev. Lett. 90 (2003) 157401.
[73] A.G. Souza Filho, A. Jorio, Anna K. Swan, M.S. Ünlü, B.B. Goldberg, R. Saito, J.H. Hafner, C.M. Lieber, M.A. Pimenta, G. Dresselhaus, M.S. Dresselhaus, Anomalous two-peak G'-band Raman effect in one isolated single-wall carbon nanotubes, Phys. Rev. B 65 (2002) 085417.
[74] A.G. Souza Filho, A. Jorio, Ge.G. Samsonidze, G. Dresselhaus, M.S. Dresselhaus, A.K. Swan, M.S. Ünlü, B.B. Goldberg, R. Saito, J.H. Hafner, C.M. Lieber, M.A. Pimenta, Probing the electronic trigonal warping effect in individual single-wall carbon nanotubes using phonon spectra, Chem. Phys. Lett. 354 (2002) 62–68.
[75] A.G. Souza Filho, A. Jorio, G. Dresselhaus, M.S. Dresselhaus, R. Saito A.K., Swan, M.S. Ünlü, B.B. Goldberg, J.H. Hafner, C.M. Lieber, M.A. Pimenta, Effect of quantized electronic states on the dispersive Raman features in individual single wall carbon nanotubes, Phys. Rev. B 65 (2002) 035404-(1–6).
[76] M.A. Pimenta, E.B. Hanlon, A. Marucci, P. Corio, S.D.M. Brown, S.A. Empedocles, M.G. Bawendi, G. Dresselhaus, M.S. Dresselhaus, The anomalous dispersion of the disorder-induced and the second-order Raman bands in carbon nanotubes, Brazilian J. Phys. 30 (2000) 423–427.
[77] H. Wilhelm, M. Lelausian, E. McRae, B. Humbert, Raman spectroscopic studies on well-defined carbonaceous materials of strong two-dimensional character, J. Appl. Phys. 84 (1998) 6552–6558.
[78] Ge.G. Samsonidze, R. Saito, A. Jorio, A.G. Souza Filho, A. Grüneis, M.A. Pimenta, G. Dresselhaus, M.S. Dresselhaus, Phonon trigonal warping effect in graphite and carbon nanotubes, Phys. Rev. Lett. 90 (2003) 027403.
[79] A.G. Souza Filho, A. Jorio, Ge.G. Samsonidze, G. Dresselhaus, R. Saito, M.S. Dresselhaus, Raman spectroscopy for probing chemically/physically induced phenomena in carbon nanotubes, Nanotechnology 14 (2003) 1130–1139, web publication: http://stacks.iop.org/0957-4484/14/1130.
[80] D.S. Knight, W.B. White, A general review about the use of Raman for diamond and diamond films, J. Mater. Res. 4 (1989) 385.

[81] Y. Kawashima, G. Katagiri, Observation of the out-of-plane mode in the Raman scattering from the graphite edge plane, Phys. Rev. B 59 (1999) 62–64.
[82] S.D.M. Brown, P. Corio, A. Marucci, M.A. Pimenta, M.S. Dresselhaus, G. Dresselhaus, Second-order resonant Raman spectra of single-walled carbon nanotubes, Phys. Rev. B 61 (2000) 7734–7742.
[83] L. Alvarez, A. Righi, T. Guillard, S. Rols, E. Anglaret, D. Laplaze, J.-L. Sauvajol, Resonant Raman study of the structure and electronic properties of SWNTs, Chem. Phys. Lett. 316 (2000) 186–190.
[84] J.M. Benoit, J.P. Buisson, O. Chauvet, C. Godon, S. Lefrant, Low-frequency Raman studies of multiwalled carbon nanotubes: experiments and theory, Phys. Rev. B 66 (2002) 073417.
[85] Y. Zhao, B.I. Yakobson, R.E. Smalley, Dynamic topology of fullerene coalescence, Phys. Rev. Lett. 88 (2002) 185501.
[86] X. Zhao, Y. Ando, L.-C. Qin, H. Kataura, Y. Maniwa, R. Saito, Radial breathing modes of multiwalled carbon nanotubes, Chem. Phys. Lett. 361 (2002) 169–174.
[87] A.M. Rao, A. Jorio, M.A. Pimenta, M.S.S. Dantas, R. Saito, G. Dresselhaus, M.S. Dresselhaus, Polarized Raman study of aligned multiwalled carbon nanotubes, Phys. Rev. Lett. 84 (2000) 1820–1823 see also Comment PRL 85 (2000) 3545.
[88] X. Zhao, Y. Ando, L.-C. Qin, H. Kataura, Y. Maniwa, R. Saito, Multiple splitting of G-band modes from individual multiwalled carbon nanotubes, Appl. Phys. Lett. 81 (2002) 2550.
[89] S. Bandow, K. Hiraoka, G. Chen, P.C. Eklund, S. Iijima, Turning peapods into double-walled carbon nanotubes, Bull. Mater. Res. Soc. 29 (2004) 260–264.
[90] V.W. Brar, Ge.G. Samsonidze, A.P. Santos, S.G. Chou, D. Chattopadhyay, S.N. Kim, F. Papadimitrakopoulos, M. Zheng, A. Jagota, G.B. Onoa, A.K. Swan, M.S. Ünlü, B.B. Goldberg, G. Dresselhaus, M.S. Dresselhaus, Resonance Raman spectroscopy characterization of single-wall carbon nanotube separation by their metallicity and diameter, J. Nanosci. Nanotechnol, in press.
[91] A. Hartschuh, E.J. Sanchez, X.S. Xie, L. Novotny, High-resolution near-field Raman microscopy of single-walled carbon nanotubes, Phys. Rev. Lett. 90 (2003) 95503.